

CFD MODELLING OF WALL JETS

A dissertation submitted to The University of Manchester for the degree of
MSc in Aerospace Engineering
in the Faculty of Science and Engineering

2022

10993691

THE SCHOOL OF ENGINEERING

LIST OF CONTENTS

List of Contents	2
List of Figures	4
Abstract	7
Declaration	8
Intellectual Property Statement	9
Acknowledgements	10
1. Introduction	11
2. Literature Review	16
2.1 3D turbulent wall jets	16
2.2 2D turbulent wall jets	20
3. Methodology	24
3.1 Governing equations	24
3.2 Turbulence models	25
3.3 Details of geometry and computational domain	28
3.4 Boundary conditions	30
3.5 Details of solver	30
3.6 Grid independence study	30
4. Results and Discussion	35
4.1 Quantities in inner scaling	35
4.1.1 Streamwise mean velocity in inner scaling	35
4.1.2 The turbulent kinetic energy (TKE) in inner scaling	42
4.1.3 Reynolds shear stress in inner scaling	43
4.2 Quantities in outer scaling	45
4.2.1 Streamwise mean velocity in outer scaling	45
4.2.2 The growth rate of the wall jet	50
4.2.3 Decay of streamwise mean velocity	51
4.2.4 The turbulent kinetic energy (TKE) in outer scaling	52
4.2.5 Reynolds shear stress in outer scaling	56

5. Conclusion	58
References	60

LIST OF FIGURES

Figure 1.1. Fully developed plane wall jet with accepted nomenclature	13
Figure 1.2. Schematic of a 3D wall jet	14
Figure 2.1. Schematic of a 3D wall jet showing regions with different rates of maximum velocity decay	16
Figure 2.2. (a) Streamwise and (b) wall-normal velocity profiles at $x/b = 10$ and $x/b = 20$, scaled with inner variables	18
Figure 2.3. A typical velocity profile in inner scaling for a turbulent boundary layer	19
Figure 3.1. Geometry with boundary conditions	29
Figure 3.2(a). Comparison of velocity profiles at $x/b = 10$	31
Figure 3.2(b). Comparison of velocity profiles at $x/b = 20$	32
Figure 3.2(c). Comparison of velocity profiles at $x/b = 150$	32
Figure 3.3(a). Comparison of TKE profiles at $x/b = 10$	33
Figure 3.3(b). Comparison of TKE profiles at $x/b = 20$	33
Figure 3.3(c). Comparison of TKE profiles at $x/b = 150$	33
Figure 3.4 Comparison of wall y^+ for different meshes	34
Figure 3.5 Computational domain generated in ANSYS meshing	34
Figure 4.1. Streamwise mean velocity profile in inner scaling at $x/b = 10$	35
Figure 4.2. Streamwise mean velocity profile in inner scaling at $x/b = 20$	35
Figure 4.3 Streamwise mean velocity profile in inner scaling at $x/b = 40$	36
Figure 4.4(a). Wall shear stress comparison	37
Figure 4.4(b). Wall shear stress in the inlet region	38
Figure 4.5(a). Wall y^+ comparison	38
Figure 4.5(b). Wall y^+ in the inlet region	38

Figure 4.6. Streamwise mean velocity profile in inner scaling at $x/b = 70$	40
Figure 4.7. Streamwise mean velocity profile in inner scaling at $x/b = 100$	40
Figure 4.8. Streamwise mean velocity profile in inner scaling at $x/b = 150$	40
Figure 4.9. Streamwise mean velocity profile in near wall region at $x/b = 100$	41
Figure 4.10. Streamwise mean velocity profile in inner scaling at $x/b = 100$	42
Figure 4.11. TKE profile in inner scaling at $x/b = 70$	42
Figure 4.12. Reynolds shear stress profile in inner scaling at $x/b = 10$	43
Figure 4.13. Reynolds shear stress profile in inner scaling at $x/b = 20$	44
Figure 4.14. Reynolds shear stress profile in inner scaling at $x/b = 40$	44
Figure 4.15. Streamwise mean velocity profile in outer scaling at $x/b = 10$	46
Figure 4.16. Streamwise mean velocity profile in outer scaling at $x/b = 20$	46
Figure 4.17. Streamwise mean velocity profile in outer scaling at $x/b = 30$	47
Figure 4.18. Streamwise mean velocity profile in outer scaling at $x/b = 40$	47
Figure 4.19. Streamwise mean velocity profile in outer scaling at $x/b = 70$	48
Figure 4.20. Streamwise mean velocity profile in outer scaling at $x/b = 100$	48
Figure 4.21. Streamwise mean velocity profile in outer scaling at $x/b = 150$	49

Figure 4.22. Streamwise mean velocity profile in outer scaling at $x/b = 200$	49
Figure 4.23. Jet growth rate along the streamwise direction	50
Figure 4.24. Maximum streamwise mean velocity decay	51
Figure 4.25. TKE profile in outer scaling at $x/b = 10$	52
Figure 4.26. TKE profile in outer scaling at $x/b = 20$	52
Figure 4.27. TKE profile in outer scaling at $x/b = 30$	53
Figure 4.28. TKE profile in outer scaling at $x/b = 40$	53
Figure 4.29. TKE profile in outer scaling at $x/b = 70$	54
Figure 4.30. TKE profile in outer scaling at $x/b = 100$	54
Figure 4.31. TKE profile in outer scaling at $x/b = 150$	55
Figure 4.32. TKE profile in outer scaling at $x/b = 200$	55
Figure 4.33. Reynolds shear stress profile in outer scaling at $x/b = 70$	56
Figure 4.34 Reynolds shear stress profile in outer scaling at $x/b = 100$	57
Figure 4.35 Reynolds shear stress profile in outer scaling at $x/b = 150$	57

LIST OF TABLES

Table 1. Comparison between the turbulence model predicted and the experimental values of normalised friction velocity and maximum streamwise mean velocity location at $x/b = 10$	39
Table 2. Comparison of streamwise rate of the spread between $x/b = 20$ and $x/b = 200$	51

ABSTRACT

A two-dimensional turbulent wall jet in a quiescent surrounding was modelled using Reynolds averaged Navier Stokes (RANS) based turbulence models available in the ANSYS Fluent 2020R2 software. The Reynolds number of the jet, $Re = 9600$, is based on jet inlet height, b and inlet velocity, U_0 . The objective was to perform a comparative study and determine the most suitable turbulence model to simulate a turbulent wall jet, which has many industrial applications.

The computational domain and boundary conditions were selected to mimic the experiment by Eriksson et al. (1998). The grid had 400 cells in the streamwise direction and 150 cells in the wall-normal direction. Nine turbulence models, including the standard $k - \varepsilon$, RNG $k - \varepsilon$, realizable $k - \varepsilon$, standard $k - \omega$, SST $k - \omega$, RSM LPS, RSM QPS, RSM stress BSL and RSM stress omega were utilized for the numerical modelling.

Profiles of streamwise mean velocity, turbulent kinetic energy and Reynolds shear stress scaled with the inner and outer variable in the initial development and fully developed region were compared for each turbulence model. Additionally, streamwise jet growth rate and mean velocity decay were also compared. Finally, the efficacy of each turbulence model was determined by comparing the numerical results with experimental data by Eriksson et al. (1998).

In most cases, a good agreement was achieved between computed and corresponding experimental results. However, RSM LPS and RSM QPS produced anomalous results. All the turbulence models also struggled to capture flow features in the outermost region of the flow $y/y_{1/2} > 1$ and also could not predict the inner peak of turbulent kinetic energy at $x/b = 70$ well. Nevertheless, comparisons also show that RSM stress BSL and RSM stress omega perform reasonably well at all streamwise locations away from the jet inlet and are the most suitable models among the selected ones.

DECLARATION

I, Rohin Kappillil Rajeev, hereby declare that this dissertation report entitled CFD Modelling of Wall Jets is my original work carried out under Dr Timothy Craft, Senior Lecturer at The University of Manchester, UK. I also declare that no portion of the work referred to in the dissertation has been submitted to support an application for another degree or qualification from this or any other university or institute of learning.

INTELLECTUAL PROPERTY STATEMENT

- i. The author of this dissertation (including any appendices and/or schedules to this dissertation) owns certain copyright or related rights in it (the “Copyright”) and s/he has given The University of Manchester certain rights to use such Copyright, including for administrative purposes.
- ii. Copies of this dissertation, either in full or in extracts and whether in hard or electronic copy, may be made only in accordance with the Copyright, Designs and Patents Act 1988 (as amended) and regulations issued under it or, where appropriate, in accordance with licensing agreements which the University has entered into. This page must form part of any such copies made.
- iii. The ownership of certain Copyright, patents, designs, trademarks and other intellectual property (the “Intellectual Property”) and any reproductions of copyright works in the dissertation, for example graphs and tables (“Reproductions”), which may be described in this dissertation, may not be owned by the author and may be owned by third parties. Such Intellectual Property and Reproductions cannot and must not be made available for use without the prior written permission of the owner(s) of the relevant Intellectual Property and/or Reproductions.
- iv. Further information on the conditions under which disclosure, publication and commercialisation of this dissertation, the Copyright and any Intellectual Property and/or Reproductions described in it may take place is available in the University IP Policy, in any relevant Dissertation restriction declarations deposited in the University Library, and The University Library’s regulations.

ACKNOWLEDGEMENTS

I want to take this opportunity to offer my sincere gratitude to everyone who assisted me in finishing this project successfully.

I am incredibly grateful to my supervisor, Dr Timothy Craft, Senior Lecturer in the Department of Mechanical, Aerospace, and Civil Engineering at The University of Manchester, for his excellent guidance, support and constructive feedback. In addition, I want to thank Dr Ciara McGrath, lecturer in aerospace systems at The University of Manchester, for her continuous support throughout the academic year.

I want to thank my family members, especially my parents, for their unconditional support and blessings, which helped me to reach this position. Furthermore, I owe a special thanks to my friends back home for their motivation and moral support. Finally, I thank the Almighty for the blessings showered upon me.

1. INTRODUCTION

“An ideal model should introduce the minimum amount of complexity while capturing the essence of the relevant physics,” wrote D.Wilcox (2008) in his book “Turbulence Modelling for CFD”. Many turbulence models widely employed in today’s practical applications are based on this core idea. Through the use of mathematical formulas, turbulence models attempt to replicate physics. Turbulence models are validated using a variety of test cases and well-defined experimental data before becoming accepted by researchers. Flat plate boundary layers, free shear flows, wall jets, backwards-facing steps, channel flow, adverse pressure gradient flows, shock-induced flow separation, and flows ranging from incompressible to hypersonic are examples of such test cases.

Currently, turbulence can be modelled using the Reynolds Averaged Navier Stokes (RANS) equations or simulated using Direct Numerical Simulation (DNS) and Large Eddy Simulation (LES). Direct Numerical Simulation (DNS) tries to solve for the three-dimensional and time-dependent solution of the Navier Stokes equations, which provides the most accurate solution of the equations numerically. Large Eddy Simulation (LES) attempts to capture large eddy scales as they contribute more to turbulence, whereas the smaller scales are modelled.

RANS modelling involves time averaging the Navier Stokes equations, so the information about the instantaneous flow is lost. In addition, time averaging introduces a new term in the Navier Stokes equations called the Reynolds stress tensor. RANS method models the effect of all the turbulent eddy scales and requires extensive closure modelling.

Reynolds stresses can be determined using the Boussinesq hypothesis or modelled Reynolds stress transport equations. According to the Boussinesq hypothesis, mean velocity gradients and turbulent viscosity are related to Reynolds stresses. This approximation gives the Linear Eddy Viscosity models such as the Mixing length model (zero-equation), Spalart-Allmaras model (one-equation), $k - \varepsilon$ model (two-equation) and $k - \omega$ model (two-equation). There are three variants of the $k - \varepsilon$ model tested in this

work – standard, realizable and RNG models. The standard $k - \omega$ and shear stress transport (SST) $k - \omega$ models are also tested in this work.

Reynolds stresses can also be found using the exact Reynolds stress transport equations, although models have to be introduced for pressure strain, dissipation and turbulent diffusion in order to close these equations. This turbulence model is called the Reynolds stress model (RSM). RSM has different variants depending on how the terms are modelled. Four RSMs have been tested in the present work. They are linear pressure strain (LPS), quadratic pressure strain (QPS), stress baseline (BSL) and stress omega.

Compared to RANS, DNS and LES give more detailed results, but they demand a lot of computational resources. DNS gives the best representation of the full Navier Stokes equations without turbulence modelling. So, all scales of motion are captured. The computational cost of performing DNS is approximately proportional to $Re^{9/4}$ where Re is the Reynolds number. This dependence of DNS on Reynolds number makes high Reynolds number simulations very computationally intensive. For LES, closure modelling is required for Kolmogorov scales of motion and hence could be considered less computationally expensive than DNS.

In the past, it was challenging to carry out high-fidelity simulations like DNS and LES at high Reynolds numbers, but recently, this has become more of an option because of the rapid development in processing capabilities. However, the cost of this computing capability is substantial, and it consumes many CPU hours. Considering this, DNS and LES are currently restricted to well-funded research programmes and are not appropriate for use in industrial applications.

For CFD applications in the industry, getting reasonably accurate results within a budget and time frame is crucial. There is always a trade-off between accuracy, time and available resources that needs to be considered. Thus, RANS could be more suitable for modelling industrial flows as it is much cheaper than DNS and LES, and industrial flow simulations do not require very fine flow features. CFD is more widely utilised than ever to simulate flows with several practical applications. The turbulent wall jet is one type of such flow.

A wall jet may be defined as “a shear flow directed along a wall, where, by virtue of the initially supplied momentum, at any station, the streamwise velocity over some region within the shear flow exceeds that in the external stream” (Launder and Rodi, 1983). In simple terms, wall jets are created when a fluid jet is blown across a surface at a higher velocity than the ambient flow. The interaction of the boundary layer and the shear jet layer gives these jets their primary flow feature. The first layer, often known as the inner layer, originates from the boundary layer along the wall due to the fluid’s high momentum. Then, between the high-velocity fluid and the ambient flow, which has a different velocity than the jet, a second layer called the outer layer forms (Naqavi et al., 2018).

The interaction of the inner and outer layers produces turbulence and a complicated flow field. This interaction between two near-wall layers, a unique and fascinating property, has piqued researchers’ curiosity to learn more about it. Figure 1.1 shows a sketch of a plane wall jet.

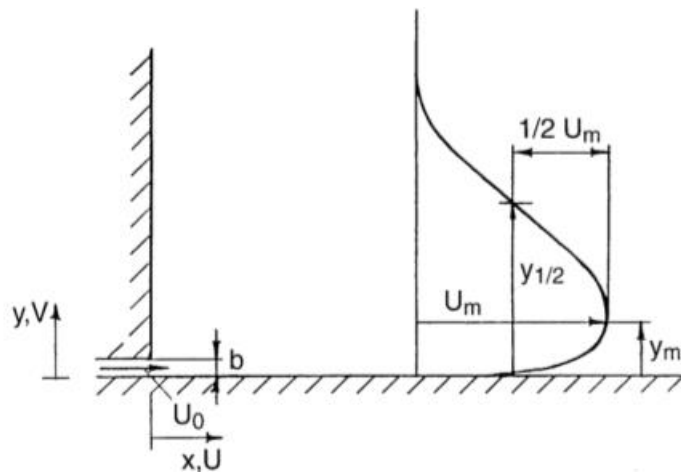


Figure 1.1 Fully developed plane wall jet with accepted nomenclature (Eriksson, 1998)

The quick spanwise spread compared to that normal to the wall is a fascinating property of the three-dimensional(3D) wall jet. A 3D wall jet is shown in Figure 1.2.

Furthermore, wall jets have a wide range of engineering and environmental applications. For example, we can find applications of wall jets in the film cooling of primary stages and combustion chamber of gas turbines, automobile window defrosters, drying of racetracks, and exhaust design of vehicles. However, applications are not just limited to these. The

study of wall jets is essential to improve the efficiency of processes involving heating, cooling, and drying surfaces. (Fu et al., 2016)

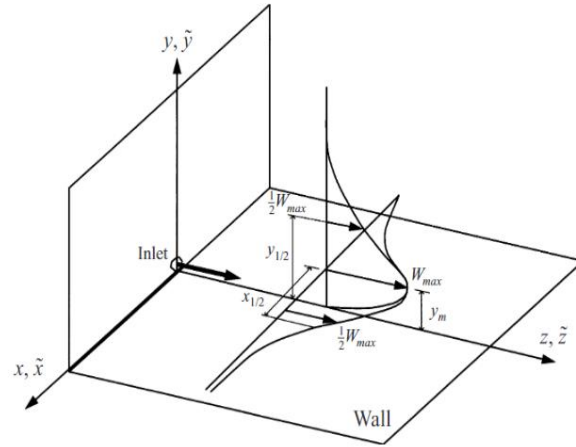


Figure 1.2 Schematic of a 3D wall jet (Craft and Launder, 2001)

Studies related to wall jets are also applied to flow separation control devices. In such cases, the objective is to inject a high momentum fluid into the near-wall region to reduce the flow separation. However, we require minimum mixing in most cases of film cooling applications. (Naqavi et al., 2018)

There are several different versions of $k - \varepsilon$ models, $k - \omega$ models, and RSMs, depending on the transport equations used to find turbulent kinetic energy k , dissipation rate ε and specific dissipation rate ω or value of model constants used. No turbulence model is perfect, and each has advantages and limitations. For example, a turbulence model might be more widely used for a specific case because of its ability to compute more accurate flow properties than other models. Various investigations have been carried out to compare the difference in accuracy between different types of simulations.

Wall jets have been extensively investigated in the past, both experimentally and numerically. In addition, various researchers have used DNS, LES and RANS modelling over the years.

It is necessary to find the most accurate RANS turbulence model for modelling turbulent wall jets as they have numerous industrial applications. This work used experimental data from Eriksson et al. (1998) to examine the accuracy of different turbulence models in

commercial CFD software, ANSYS Fluent. CFD software like ANSYS Fluent allows anyone to perform numerical analysis of various flows. They have a clean user interface using which the problem can be set up and numerically solved. As mentioned, a range of prominent turbulence models is included in the package to model turbulent flows. Numerical results were exported to MATLAB for visualising. Free windows-based software called WebPlotDigitizer was used to extract data from Eriksson et al. (1998).

2. LITERATURE REVIEW

Various researchers have looked into wall jets under various configurations and flow conditions. Jets along the wall and offset from the wall, jets with an isothermal or adiabatic wall, a backwards-facing step, and jet impingement are only a few examples. Particle Image Velocimetry (PIV), Laser Doppler Velocimetry (LDV), and hotwire anemometer have been utilised to obtain measurements. The LES, DNS, and other RANS turbulence models were employed in the numerical calculations. In the past, 3D and 2D turbulent wall jets have been investigated. In addition, the effect of the shape of the input nozzle on flow characteristics was investigated in some research studies. Furthermore, the inlet Reynolds number of the flow may vary between investigations.

2.1 3D turbulent wall jets

In 1970, Sforza and Herbst reported one of the first experimental 3D incompressible turbulent wall jets in a quiescent ambient condition with rectangular orifices having aspect ratios of 0.025, 0.05, 1 and 10 and an orifice area of 1 in². They concluded that the maximum velocity decay in the radial type decay region (shown in Figure 2.1) was closely proportional to $x^{-1.10}$ for all cases of aspect ratios selected, where x is the streamwise coordinate. This finding showed that the geometry of the jet inlet did not affect the spread rate of the jet in a normal to the wall direction and streamwise centerline velocity decay far enough downstream.

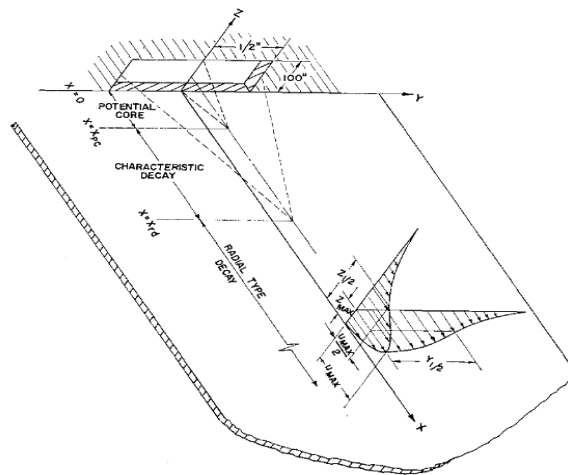


Figure 2.1 Schematic of a 3D wall jet showing regions with different rates of maximum velocity decay. (Sforza and Herbst, 1970)

Newman et al. (1972) used a long domain to acquire a fully developed flow of a 3D wall jet using a circular jet inlet. Experimental tests were performed using air and water with Reynolds numbers between 16400 and 2800. They discovered that the wall-normal spread rate in planar wall jets is higher than in 3D wall jets, although the streamwise turbulence intensity is higher in 3D wall jets. They also discovered that the spread rate in the spanwise direction is more extensive than in the wall-normal direction for a 3D wall jet.

Launder and Rodi (1981,1983) reviewed scientific developments in turbulent wall jets until 1980. The same authors noted that the spread rate in the perpendicular direction to the wall is about 5.5 times lower than the spread rate parallel to the wall in a 3D wall jet.

Craft and Launder (2001) suggested that substantial spreading of the wall jet along the wall is caused by the development of streamwise vorticity and not due to anisotropic diffusion. They also concluded that Reynolds stress plays a significant role in the lateral spread of the wall jet, and it is the source of the streamwise vorticity. Further, they proposed the possibility of incomplete flow development in the experimental data available until then.

Dejoan and Leschziner (2005) used LES to compare velocity profiles and turbulence properties for a planar turbulent wall jet in quiescent surroundings with the experimental results of Eriksson et al. (1998). The Reynolds number of the jet was taken as 9600 based on inlet jet velocity and slot height, identical to that in the experiment. They also studied the budgets of Reynolds stresses and turbulent kinetic energy, which provided better insights into the transition between the outer shear layer and the boundary layer. LES and experimental data showed close agreement. However, they stated that the LES technique is unable to accurately capture the transition between the outer shear layer and the boundary layer, which explains the discrepancy between the experimental results of Eriksson et al. (1998) and LES in the $60 < y^+ < 400$ regions, as shown in Figure 2.2.

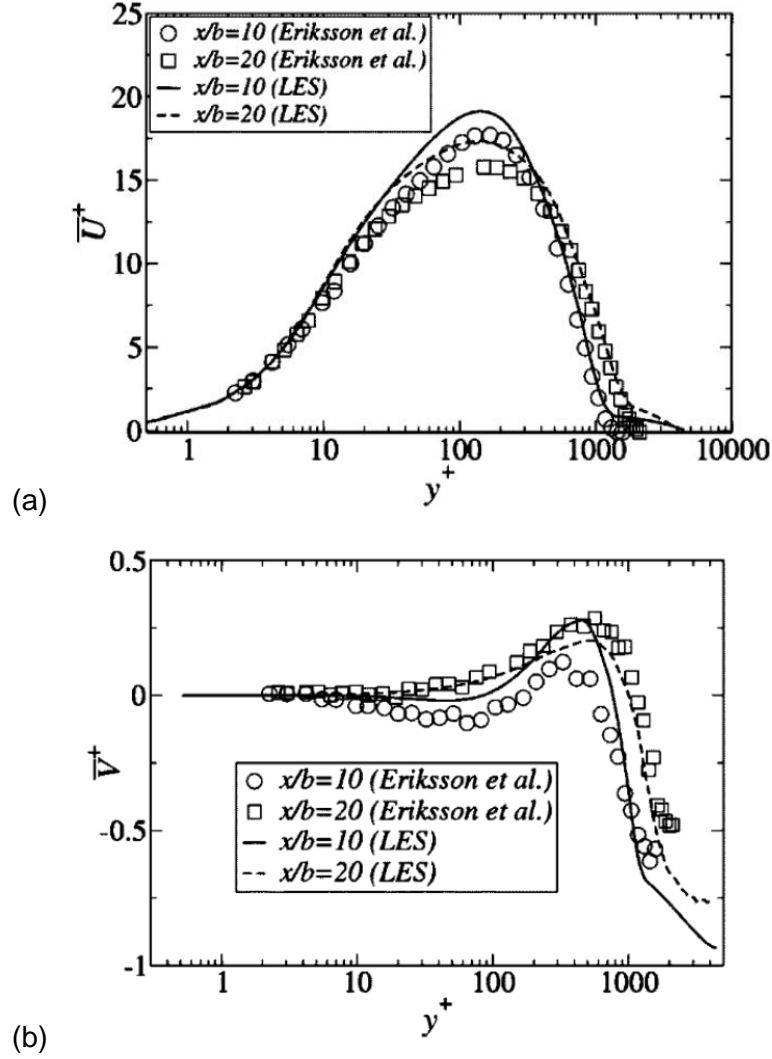


Figure 2.2 (a) Streamwise and (b) wall-normal velocity profiles at $x/b = 10$ and $x/b = 20$, scaled with inner variables. (Dejoan and Leschziner, 2005)

Measurements near solid boundaries in turbulent flows show that for internal and external flows, the streamwise velocity in the flow near the wall varies logarithmically with distance from the surface. This relation is called the law of the wall. (Wilcox, 2006)

$$\frac{U}{U_\tau} = \frac{1}{\kappa} \ln \frac{y U_\tau}{\nu} + C \quad (1)$$

where $C \approx 5.0$ for smooth surfaces and $\kappa \approx 0.41$ for smooth and rough surfaces

or in general,
$$U = U_\tau f(y^+) \quad (2)$$

Non-dimensional distance from the wall is given by,

$$y^+ = \frac{yU_\tau}{\nu} \quad (3)$$

$$U^+ = \frac{U}{U_\tau} \quad (4)$$

where y is the wall-normal coordinate, U is the velocity component in the streamwise coordinate and ν is the kinematic viscosity

$$\text{friction velocity } U_\tau = \sqrt{\frac{\tau_\omega}{\rho}} \quad (5)$$

where τ_ω is the wall shear stress and ρ is the density

$$\text{wall shear stress } \tau_\omega = \mu \left(\frac{\partial u}{\partial y} \right)_{y=0} \quad (6)$$

where μ is the dynamic viscosity

For $y^+ < 5$, $U^+ = y^+$ and when $30 < y^+ < 300$, the velocity profile matches the law of the wall, as shown in Figure 2.3. The log layer is where the viscous sublayer and the defect layer merge, and the velocity profile is the same as the law of the wall. (Wilcox,2006)

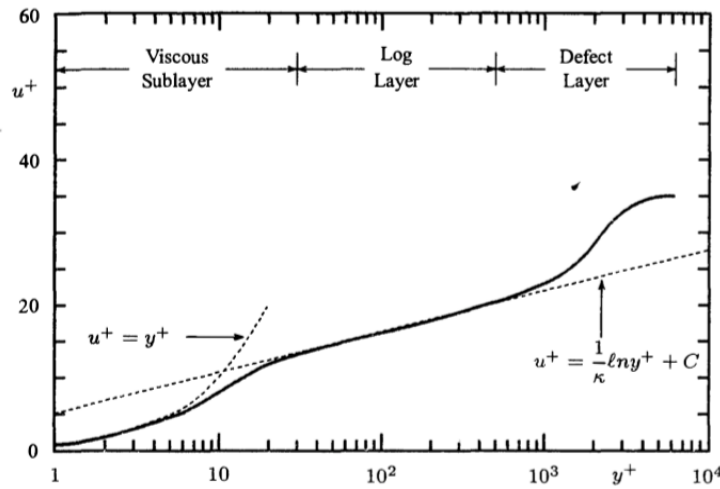


Figure 2.3 A typical velocity profile in inner scaling for a turbulent boundary layer (Wilcox,2006)

Researchers observed that a fully developed turbulent wall jet would show jet behaviour similar to that of a flat plate turbulent boundary layer and identified a short region where the log law is satisfied. Eriksson et al. (1998) and Dejoan and Leschziner (2005) are a few to observe this region. This region could be verified from the inner scaled streamwise mean velocity profiles from the numerical results.

The DNS of a 3D turbulent wall jet was done at a Reynolds number of 7500 by Naqavi et al. (2018). They found that the turbulent diffusion interacts with the inner and outer layers, causing excess energy from the perpendicular direction of the wall to be transferred to the spanwise direction.

An experimental investigation was performed by Godi et al. in 2019 to gain more knowledge on the effect of inlet geometry on the flow and heat transfer characteristics of a 3D wall jet at a Reynolds number of 7500 based on the hydraulic diameter of inlet and inlet jet velocity. The effect of inlet geometry on the flow and heat transfer characteristics was observed close to the jet exit, and the size of the jet inlet affected the average Nusselt number significantly.

To characterise the flow and thermal characteristics of a 3D turbulent wall jet at Reynolds number 7500, Kakka and Anupindi (2021) used the LES method. The evolution and contribution to the spanwise spread of the mean streamwise and wall-normal vorticity components were investigated. These components were discovered to contribute to the jet's significant spanwise dispersion.

2.2 2D turbulent wall jets

Schneider and Goldstein (1994) experimented with using Laser Doppler Velocimetry (LDV) to measure the turbulence characteristics of a 2D planar wall jet with a Reynolds number of 14000 based on inlet width. They compared results from this experiment with previously performed hot wire studies and confirmed that mean velocity profiles, decay and growth rates matched well. However, the values of normal Reynolds stresses $\langle u_i^2 \rangle$ and $\langle u_j^2 \rangle$ produced were higher than hot wire data.

Eriksson et al. conducted numerous experimental tests on wall jets during the 1990s. In 1998, they used Laser Doppler Velocimetry (LDV) to take measurements in a planar

turbulent wall jet attached to the wall at a Reynolds number of 9600 based on inlet slot height and inlet jet velocity. They investigated the initial development and fully developed condition of the flow, giving more focus on the inner area of the flow ($y^+ < 4$) to determine wall shear stresses accurately. Mean velocity profiles and turbulence quantities of fully developed flow in outer and inner scaling were studied in detail. This work is commonly used to validate numerical models. (Dejoan and Leschziner, 2005; Rathore and Das, 2013; Fu et al., 2016; Yan et al., 2018)

Low Reynolds number $k - \varepsilon$ models at varying Reynolds numbers (22500 to 7300) based on inlet jet velocity were employed by Kechiche et al. in 2004 to study turbulent 2D plane wall jets in the quiescent environment. Measurements from the literature (Tailland 1970 and Karlsson et al. 1992) were used to validate the findings. In addition, they claimed that Ljuboja and Rodi's (1980) turbulence models accorded with experimental evidence sufficiently in the case of isothermal walls.

Rostamy et al. (2011) researched the effect of surface roughness on the mean velocity and skin friction parameters of turbulent wall jets over smooth and rough surfaces at a Reynolds number of 7500, based on inlet slot height and inlet jet velocity. A 36-grit sheet provided the rough surface. They observed that the spread rate of the jet was not affected by the rough surface, and the streamwise decay rate of the maximum velocity and inner layer thickness increased. An in-depth study by Tang et al. (2015) revealed that surface roughness affected flow characteristics of both inner and outer layers, but the effect on the outer region was relatively small.

Balabel and El-Askary carried out a numerical study in 2011 of many linear and non-linear $k - \varepsilon$ turbulence model versions in diverse jet flow applications. A plane turbulent wall jet was simulated at a Reynolds number of 9600 based on inlet slot height and inlet jet velocity. After comparing numerical findings with experimental data from Eriksson et al. (1998), the authors determined that linear turbulence models produced good results in simple, non-impinging jet flows. However, impinging and wall jets were predicted better by non-linear turbulence models.

In 2011, Tahsini evaluated the accuracy of the Spalart-Allmaras turbulence model in the numerical analysis of a 2D turbulent wall jet with Reynolds number 18000 based on inlet

height and inlet jet velocity. The fluid and thermal behaviour of the turbulence model was investigated using adiabatic and uniform heat flux conditions for the wall. They noted that the numerical results for the adiabatic wall case and the experimental data from Tailland (1970) were in good agreement. In addition, they concluded that the Spalart-Allmaras turbulence model was suitable for industrial simulations as it takes less computational time than other models selected in their study.

Rathore and Das (2013) examined two low Reynolds number turbulence models for the fluid flow investigation of wall-bound jets. First, flow fields and turbulence properties of a planar turbulent wall jet with offset ratio 7 at Reynolds number of 15000 were compared with the measurements of Pelfrey and Liburdy (1986). The computational findings produced from Launder and Sharma's (1974) and Yang and Shih's (1993) low Reynolds number turbulence models were compared to the standard $k - \varepsilon$ model. While both models effectively simulated turbulence behaviour, low-Reynolds number modelling constructed the turbulent boundary layer and accurately resolved the near-wall field. Finally, they concluded that Yang and Shih's low Reynolds number $k - \varepsilon$ model outperformed the others.

According to Fu et al. (2016), 2D RANS simulations accord well with Eriksson et al. (1998) experimental data, and the standard $k - \varepsilon$ model with a two-layer technique delivers the most accurate results among the models tested, namely standard $k - \varepsilon$ model with two-layer wall treatment, the realizable $k - \varepsilon$ model with two-layer wall treatment, the standard $k - \omega$ model with all y^+ wall treatment and SST $k - \omega$ model with all y^+ treatment. Offset ratios of 0.5, 1.0, 1.5 and 2.0 were also considered. Further analysis revealed that as offset distance was increased, the reattachment point moved in the streamwise direction and the streamwise velocity at the reattachment point decreased.

Choosing a suitable method and producing accurate results under different flow or boundary conditions is difficult. After thoroughly understanding the published literature, we can see that in academic research, RANS-based simulations are not preferred nowadays for studying turbulent wall jets due to inaccuracies in modelling. However, for analysing industrial flows, the primary choice is RANS due to its quick calculations and reasonably good accuracy. Numerical methods such as LES and DNS require high

computational power to resolve very dense grids while taking a long time to process. Hence, it is essential to find out which RANS turbulence model in a commercial CFD package such as ANSYS Fluent can produce the most accurate results, especially in problems such as wall jets. Increasing the efficiency of wall jets can be beneficial in reducing power consumption in industrial processes and other applications

From the numerical results of ANSYS Fluent, flow parameters such as velocity profiles, Reynolds shear stresses and turbulent kinetic energy at different locations, along with jet growth rate and streamwise velocity decay, can be compared and validated using data from Eriksson et al. (1998). The accuracy of Reynolds shear stress profiles is essential as the shear stress is the main stress component that affects the streamwise mean velocity U in such 2D turbulent flows.

3. METHODOLOGY

3.1 Governing equations

At an inlet Reynolds number of 9600, numerical simulations of a turbulent, two-dimensional wall jet were performed. With the help of the ANSYS Fluent solver, two-dimensional steady Reynolds Averaged Navier Stokes (RANS) equations were solved. The standard $k - \varepsilon$ model, RNG $k - \varepsilon$ model, realizable $k - \varepsilon$ model, standard $k - \omega$ model, and SST $k - \omega$ model are all two-equation turbulence models that were used in simulations. In addition, the five equation Reynolds Stress Model (RSM) variants such as Linear Pressure-Strain model, Quadratic Pressure-Strain model, Stress Omega, and Stress BSL were also used to model the Reynolds stresses directly. Two equation models use Boussinesq approximation to model Reynolds stresses, whereas the Reynolds stress model does not.

The instantaneous pressure and velocity fields are divided into mean and fluctuation components, and the governing and transport equations are time-averaged or phase-averaged to get the RANS equations. The finer details of the flow are lost in the process. Using Einstein's compact notation, the resulting Reynolds Averaged Navier Stokes equations are expressed as follows:

Continuity equation:
$$\frac{\partial U_i}{\partial x_i} = 0 \quad (7)$$

Momentum equation:
$$\frac{\partial U_i}{\partial t} + \frac{\partial (U_i U_j)}{\partial x_j} = -\frac{1}{\rho} \frac{\partial P}{\partial x_i} + \frac{\partial}{\partial x_j} \left(\nu \frac{\partial U_i}{\partial x_j} - \overline{u_i u_j} \right) \quad (8)$$

where U_i is mean or averaged part of velocity, and u_i is fluctuating part of velocity. Molecular viscosity is given by ν , and density fluid is given by ρ

If the RANS equations for turbulent flow are compared to the Navier stokes equations for laminar flow, the only difference is the presence of the additional term $-\overline{u_i u_j}$, which is called the Reynolds stress tensor. Hence, this term can not be neglected or ignored. However, these Reynolds stresses are unknown, and different turbulent models are introduced to predict them accurately.

The linear eddy viscosity models are the most often used turbulence models. The Reynolds stresses $-\overline{u_i u_j}$ act like an additional viscous term in Equation (8). Therefore, the Reynolds stresses are represented by a quantity known as turbulent viscosity ν_t and mean velocity gradients.

$$\text{Reynolds shear stresses} \quad \overline{u_i u_j} = -\nu_t \left(\frac{\partial u_i}{\partial x_j} + \frac{\partial u_j}{\partial x_i} \right) + (2/3)k\delta_{ij} \quad (9)$$

where δ_{ij} is the Kronecker delta, which is defined as follows:

$$\delta_{ij} = \begin{cases} 1, & \text{if } i = j \\ 0, & \text{if } i \neq j \end{cases} \quad (10)$$

and k is the turbulent kinetic energy, given as:

$$k = (\overline{u_1^2} + \overline{u_2^2} + \overline{u_3^2})/2 \quad (11)$$

Now the only unknown term is the turbulent viscosity ν_t . Different models solve one or more transport equations for turbulent quantities such as turbulent kinetic energy k , turbulent kinetic energy dissipation rate, ε , and specific turbulent kinetic energy dissipation rate, ω , to determine turbulent viscosity ν_t .

3.2 Turbulence Models

In a $k - \varepsilon$ based model by Launder and Spalding (1974), in addition to the Navier Stokes equations, two equations are solved- one for TKE k and one for the dissipation rate ε . The equations are as follows

$$\frac{\partial k}{\partial t} + U_i \frac{\partial k}{\partial x_i} = p_k - \varepsilon + \frac{\partial}{\partial x_j} \left[\left(\nu + \frac{\nu_t}{\sigma_k} \right) \frac{\partial k}{\partial x_j} \right] \quad (12)$$

$$\frac{\partial \varepsilon}{\partial t} + U_i \frac{\partial \varepsilon}{\partial x_i} = c_{\varepsilon_1} \frac{\varepsilon}{k} p_k - c_{\varepsilon_2} \frac{\varepsilon^2}{k} + \frac{\partial}{\partial x_j} \left[\left(\nu + \frac{\nu_t}{\sigma_\varepsilon} \right) \frac{\partial \varepsilon}{\partial x_j} \right] \quad (13)$$

$$\text{and then turbulent viscosity is found using:} \quad \nu_t = c_\mu k^2 / \varepsilon \quad (14)$$

Constants c_{ε_1} , c_{ε_2} , c_μ , σ_ε can be varied according to the flow under study. These are widely accepted as $c_{\varepsilon_1} = 1.44$, $c_{\varepsilon_2} = 1.92$, $c_\mu = 0.09$, $\sigma_\varepsilon = 1.3$, $\sigma_k = 1.0$

$$\text{Turbulence production term,} \quad p_k = \tau_{ij} \frac{\partial u_i}{\partial x_j} \text{ or } p_k = 2\nu_t S_{ij} S_{ij} \quad (15)$$

where mean strain rate,

$$S_{ij} = \frac{1}{2} \left(\frac{\partial U_i}{\partial x_j} + \frac{\partial U_j}{\partial x_i} \right) \quad (16)$$

In the realizable $k - \varepsilon$ model by Shih et al. (1995), the constant c_μ is defined as a function of mean flow and turbulence quantities.

$$c_\mu = \frac{1}{A_0 + A_s(kU^*/\varepsilon)} \quad (17)$$

where the constants $A_0 = 4.0$ and $A_s = \sqrt{6} \cos \phi$, $\phi = (1/3) \cos^{-1}(\sqrt{6}W)$ (18)

$$W = (S_{ij}S_{jk}S_{ki})/\hat{S}^3 \quad (19)$$

$$\hat{S} = \sqrt{S_{ij}S_{ij}} \quad (20)$$

In the RNG $k - \varepsilon$ model, according to Speziale and Thangam (1992), the TKE k and dissipation rate ε equations are as same as Equations (12) and (13). However, the model constants in the equations are modified to accommodate a broader range of flows having large strain rates.

The model coefficients are, $c_{\varepsilon_2} = 1.68$, $c_\mu = 0.0845$, $\sigma_\varepsilon = 0.7179$, $\sigma_k = 0.7179$ (21)

$$c_{\varepsilon_1} = 1.42 - \frac{\eta(1-\eta/\eta_0)}{1+\beta\eta^3} \text{ where } \eta = SK/\varepsilon, S = \sqrt{2S_{ij}S_{ij}}, \eta_0 = 4.38, \beta = 0.015$$

The $k - \omega$ model is a part of the two-equation family of turbulence models, which uses two equations to solve for TKE k and specific dissipation rate ω , where $\omega = \varepsilon/\kappa$. This turbulence model was initially proposed by Saffman (1970) but was popularised by Wilcox (2008).

$$\nu_t = \frac{\rho k}{\tilde{\omega}} \quad \tilde{\omega} = \max \left\{ \omega, C_{\text{lim}} \sqrt{\frac{2\bar{S}_{ij}\bar{S}_{ij}}{\beta^*}} \right\} \quad C_{\text{lim}} = \frac{7}{8} \quad (22)$$

$$\bar{S}_{ij} = S_{ij} - \frac{1}{3} \frac{\partial U_k}{\partial x_k} \delta_{ij} \quad (23)$$

Equations for TKE k and specific dissipation ω are:

$$\frac{\partial}{\partial t}(\rho k) + \frac{\partial}{\partial x_j}(\rho U_j k) = \rho \tau_{ij} \frac{\partial U_i}{\partial x_j} - \beta^* \rho k \omega + \frac{\partial}{\partial x_j} \left[\left(\nu + \sigma^* \frac{\rho k}{\omega} \right) \frac{\partial k}{\partial x_j} \right] \quad (24)$$

$$\frac{\partial}{\partial t}(\rho \omega) + \frac{\partial}{\partial x_j}(\rho U_j \omega) = \alpha \frac{\omega}{k} \rho \tau_{ij} \frac{\partial U_i}{\partial x_j} - \beta \rho \omega^2 + \sigma_d \frac{\rho}{\omega} \frac{\partial k}{\partial x_j} \frac{\partial \omega}{\partial x_j} + \frac{\partial}{\partial x_j} \left[\left(\nu + \sigma \frac{\rho k}{\omega} \right) \frac{\partial \omega}{\partial x_j} \right] \quad (25)$$

The closure coefficients are:

$$\alpha = \frac{13}{25} \beta^* = \frac{9}{100}, \sigma = \frac{1}{2}, \sigma^* = \frac{3}{5} Pr_T = \frac{8}{9} \quad (26)$$

$$\sigma_d = \begin{cases} 0, & \frac{\partial k}{\partial x_i} \frac{\partial \omega}{\partial x_j} \leq 0 \\ \sigma_{do}, & \frac{\partial k}{\partial x_i} \frac{\partial \omega}{\partial x_j} > 0 \end{cases} \quad \sigma_{do} = \frac{1}{8} \quad (27)$$

$$\beta = \beta_0 f_\beta \quad \beta_0 = 0.0708 \quad f_\beta = \frac{1+85\chi_\omega}{1+100\chi_\omega} \quad (28)$$

$$\chi_\omega = \left| \frac{\Omega_{ij} \Omega_{jk} \hat{S}_{ki}}{(\beta^* \omega)^3} \right| \quad \hat{S}_{ki} = S_{ki} - \frac{1}{2} \frac{\partial U_m}{\partial x_m} \delta_{ki} \quad (29)$$

Rotation tensor, $\Omega_{ij} = \frac{1}{2} \left(\frac{\partial U_i}{\partial x_j} - \frac{\partial U_j}{\partial x_i} \right) \quad (30)$

The SST $k - \omega$ model by Menter (1994) is a modified version of the standard $k - \omega$ model, which blends the standard $k - \omega$ model and a modified $k - \varepsilon$ model. The model switches from $k - \omega$ model in the near wall region to $k - \varepsilon$ model away from the surface. The equations for turbulent kinetic energy k and specific dissipation ω are:

$$\frac{\partial}{\partial t} (\rho k) + \frac{\partial}{\partial x_i} (\rho k U_i) = \tau_{ij} \frac{\partial U_i}{\partial x_j} - \beta^* \rho \omega k + \frac{\partial}{\partial x_j} \left[(\nu + \sigma_k \nu_t) \frac{\partial k}{\partial x_j} \right] \quad (31)$$

$$\begin{aligned} \frac{\partial}{\partial t} (\rho \omega) + \frac{\partial}{\partial x_i} (\rho \omega U_i) = & \frac{\gamma}{\nu_t} \tau_{ij} \frac{\partial U_i}{\partial x_j} - \beta^* \rho \omega^2 + \frac{\partial}{\partial x_j} \left[(\nu + \sigma_\omega \nu_t) \frac{\partial \omega}{\partial x_j} \right] \\ & + 2(1 - F_1) \rho \sigma_{\omega 2} \frac{1}{\omega} \frac{\partial k}{\partial x_j} \frac{\partial \omega}{\partial x_j} \end{aligned} \quad (32)$$

$$\phi = F_1 \phi_1 + (1 - F_1) \phi_2 \quad (33)$$

Constants of (ϕ_1)

$$\sigma_{k1} = 0.85 \quad \sigma_{\omega 1} = 0.5 \quad \beta_1 = 0.0750 \quad \beta^* = 0.09 \quad (34)$$

$$\alpha_1 = 0.31 \quad \kappa = 0.41 \quad \gamma_1 = \beta_1 / \beta^* - \sigma_{\omega 1} \kappa^2 / \sqrt{\beta^*}$$

Constants of (ϕ_2)

$$\sigma_{k2} = 1.0 \quad \sigma_{\omega 2} = 0.856 \quad \beta_2 = 0.0828 \quad (35)$$

$$\beta^* = 0.09 \quad \kappa = 0.41 \quad \gamma_2 = \beta_2 / \beta^* - \sigma_{\omega 2} \kappa^2 / \sqrt{\beta^*} \quad (36)$$

Eddy viscosity is given by,

$$\nu_t = \frac{a_1 k}{\max(a_1 \omega; \Omega F_2)} \quad (37)$$

The absolute value of vorticity F_2 is given by,

$$F_2 = \tanh(\arg_2^2) \quad (38)$$

$$\arg_2 = \max\left(2 \frac{\sqrt{k}}{0.09 \omega y}; \frac{500 \nu}{y^2 \omega}\right) \quad (39)$$

The exact transport equations for the Reynolds stresses are essential for the Reynolds stress model. To close the Reynolds stresses equations, it is necessary to introduce models for terms like pressure strain, dissipation, and turbulent diffusion. The accuracy of modelling these terms impacts the accuracy of various Reynolds stress models. Launder et al. (1975) discussed one such turbulence model in their article. The following provides the exact transport equations for the Reynolds stresses:

$$\begin{aligned} \frac{D \overline{u_i u_j}}{Dt} = & -\frac{\partial}{\partial x_k} \left[\overline{u_i u_j u_k} + \frac{P}{\rho} (\delta_{jk} u_i + \delta_{ik} u_j) - \nu \frac{\partial \overline{u_i u_j}}{\partial x_k} \right] + \frac{P}{\rho} \left(\frac{\partial U_i}{\partial x_j} + \frac{\partial U_j}{\partial x_i} \right) \\ & - 2\nu \frac{\partial u_i}{\partial x_k} \frac{\partial u_j}{\partial x_k} - \left(\overline{u_j u_k} \frac{\partial U_i}{\partial x_k} + \overline{u_i u_k} \frac{\partial U_j}{\partial x_k} \right) \end{aligned} \quad (40)$$

3.3 Details of geometry and computational domain

Figure 3.1 depicts the geometry that was adopted in the simulations. The experimental setup used by Eriksson et al. in 1998 was replicated in the computational domain. It consists of a rectangular, two-dimensional region with an inlet on the left boundary, next

to the bottom wall, and a wall on the remainder of the left boundary. The height of the jet inlet, b , is 9.6mm. The computational domain extends 7 metres horizontally and 1.45 metres vertically. x direction is called the streamwise direction, and y direction is called the wall-normal direction. Since flow begins to reach fully turbulent beyond $x \approx 20b$ and becomes self-similar beyond $x \approx 40b$ (Eriksson et al., 1998), the chosen domain length should be sufficient for analysing developed flows.

Figure 3.1 also depicts the typical velocity profile of the streamwise component of velocity. $y = y_{max}$ is the location along the wall-normal direction where the local streamwise component of velocity is equal to the local maximum of streamwise component of velocity, U_{max} . Jet half width $y = y_{1/2}$ is the height from the wall at which the local component of streamwise velocity is half the local maximum streamwise velocity.

The geometry modeller in ANSYS Workbench was used to generate the computational domain, and ANSYS meshing was used to discretize it. All simulations used a structured and orthogonal grid. A fine mesh was utilised along the wall and closer to the inlet. This refinement helps to capture the characteristics of the inner layer of the wall jet accurately. The aim was to obtain a $y^+ < 1$ for the first cell normal to the bottom wall. Moreover, the cell size gradually increases along streamwise and wall-normal directions. This gradual increase in cells reduces the total number of cells and increases computational speed. The ANSYS Fluent solver was used for simulation and post-processing.

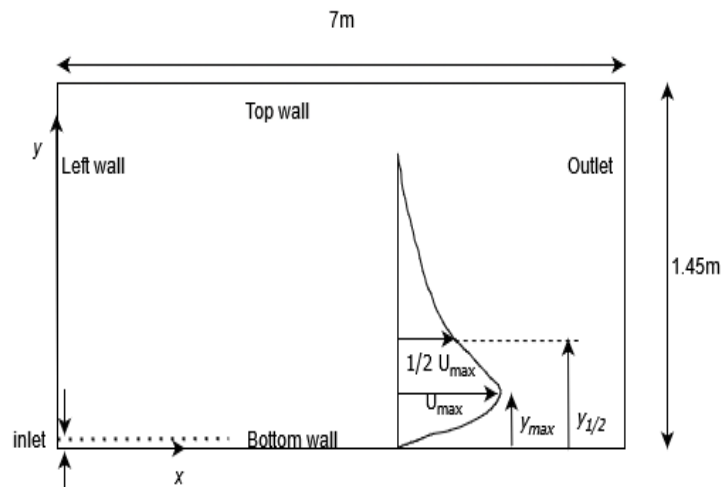


Figure 3.1 Geometry with boundary conditions (Kakka and Anupindi, 2021)

3.4 Boundary conditions

The fluid was assumed to have a density of 1kg/m^3 and a viscosity of $1\times 10^{-6}\text{ kg/m-s}$. To obtain a Reynolds number of 9600, this would equate to a mean inlet jet velocity U_0 of 1m/s. At the inlet boundary, uniform velocity conditions are applied with a 1% turbulence intensity. The turbulent length scale was assumed to be 10% of the inlet height, which gives the value of 0.96mm. No slip boundary condition was applied on the left wall and bottom wall. The pressure outlet condition was applied for the top boundary and outlet. The gauge pressure at the outlet was taken as 0 Pascal with an operating pressure of 101325 Pascal. All the simulations were performed at a Reynolds number of 9600, based on mean inlet velocity and jet inlet height, consistent with the boundary conditions used by Eriksson et al. (1998).

$$\text{Reynolds number } Re = \frac{U_0 b}{\nu} = 9600 \quad (38)$$

3.5 Details of solver

All simulations were run using the commercial CFD package ANSYS Fluent 2020R2 on a PC with a 4-core 2.3GHz Intel i5-8300H and 8 GB RAM. ANSYS Fluent is a finite volume-based CFD solver. A pressure-based steady incompressible double precision solver was employed for good accuracy and fast convergence. The least squares cell-based spatial discretization scheme was used for gradients. A second-order upwind spatial discretisation scheme was employed for momentum, TKE, and dissipation rate. The standard solution initialization was used and computed from the inlet. The solver was run to achieve a scaled residual of 1×10^{-5} for all the equations being solved. Data from the numerical results were extracted and analysed using MATLAB scripts. Vertical profiles of mean velocity and turbulence quantities scaled in outer and inner variables at locations along the streamwise direction were obtained.

3.6 Grid independence study

A grid independence analysis was done using the standard $k - \varepsilon$ to select the most suitable mesh. The profiles of parameters like the x component of velocity U and TKE were examined for five different grid arrangements. These quantities were plotted at three locations along the wall – two in the developing region and one in the fully developed

region. In the developing region, profiles of U and TKE at $x/b = 10$ and $x/b = 20$ were plotted, whereas $x/b = 150$ lies in the fully developed region. Grids have 104×280 , 130×350 , 150×400 , 180×480 , and 218×576 cells, which is given in the form $n \times m$, where n is the number of cells in the wall-normal direction and m in the streamwise direction. A grid independence study was carried out using the generated grids. At $x/b = 10, 20$ and 150 profiles of U and TKE in the outer scaling were obtained.

The profiles of normalized U velocity as a function of normalised y in the developing and developed regions are shown in Figures 3.2(a), 3.2(b) and 3.2(c). The U velocity was normalized using local maximum velocity U_{max} and the y coordinate using $y_{1/2}$. When the mesh is made more refined, there are no apparent changes in the velocity profiles at all three locations. There is a good agreement between U profiles locally in the near wall region and away from the wall.

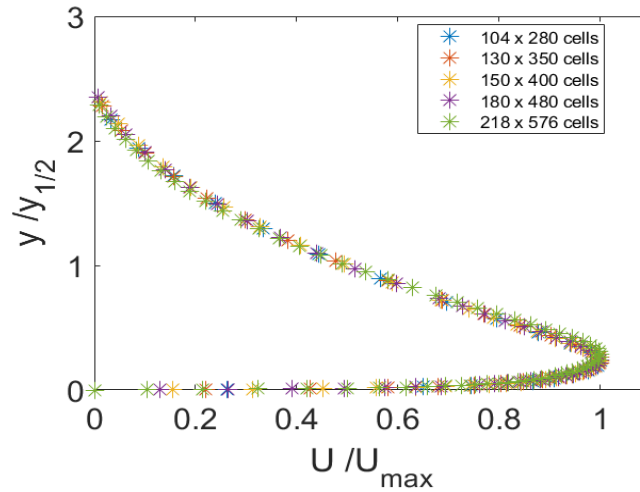


Figure 3.2 (a) Comparison of velocity profiles at $x/b = 10$

The profiles of normalized TKE as a function of normalised y in the developing and developed regions are shown in Figures 3.3(a), 3.3(b) and 3.3(c). The TKE values were normalized using U_{max}^2 . Although there are no significant changes in the results for U and TKE, when the mesh gets more refined at $x/b = 10$ and $x/b = 20$, there is a slight variation in the case of TKE. This variation might be because of the relatively coarse cells

for 104 x 280 cells mesh and gradual refinement as one moves to 218 x 576 cells mesh. From Figure 3.3(c), it can be noted that the profiles of TKE show an excellent overlap at $x/b = 150$ for all mesh resolutions. Wall y^+ less than 1 was obtained for all cases, as seen in Figure 3.4.

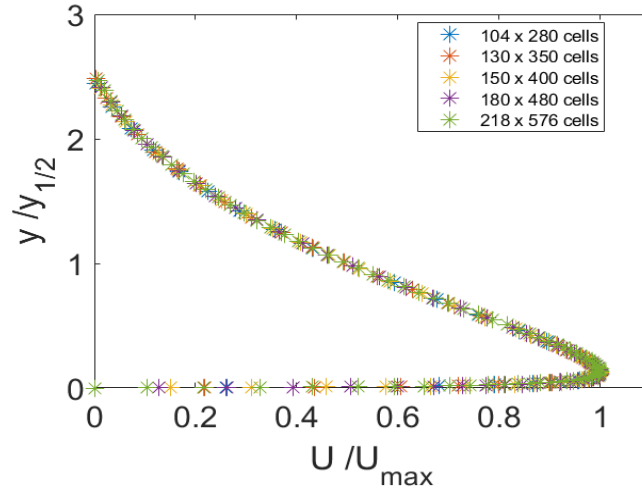


Figure 3.2(b) Comparison of velocity profiles at $x/b = 20$

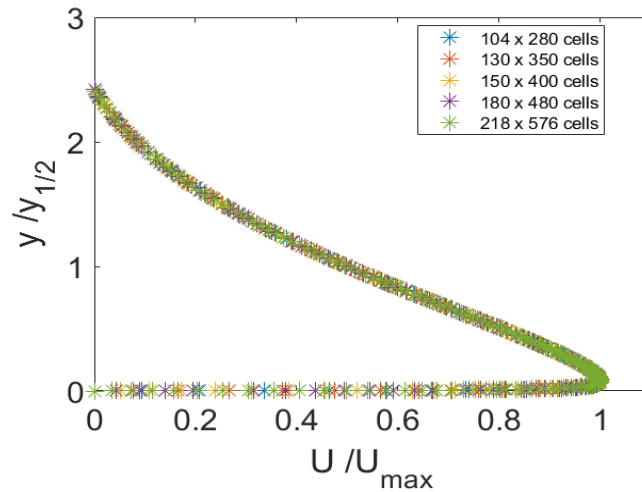


Figure 3.2. (c) Comparison of velocity profiles at $x/b = 150$

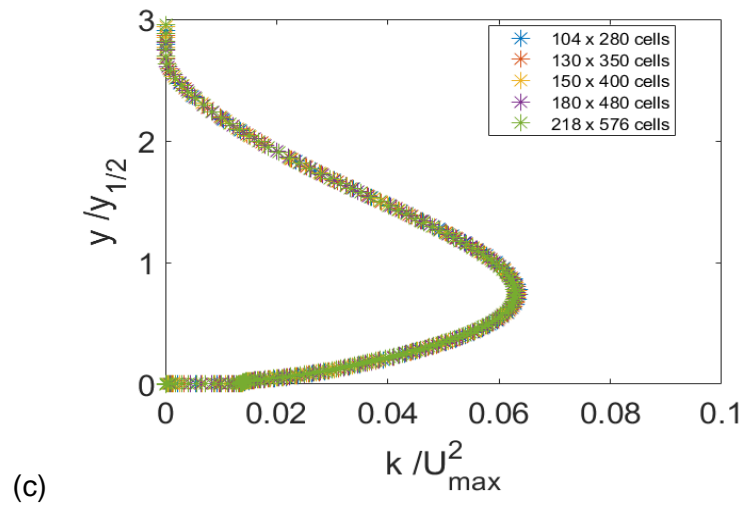
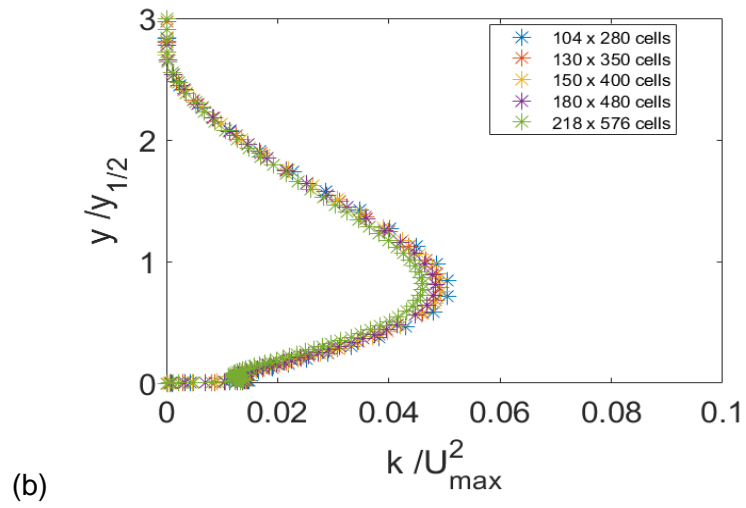
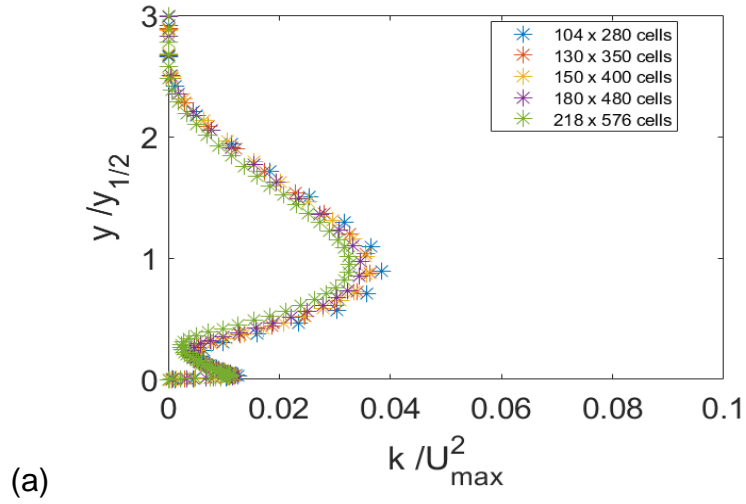


Figure 3.3 (a) Comparison of TKE profiles at $x/b = 10$. (b) Comparison of TKE profiles at $x/b = 20$. (c) Comparison of TKE profiles at $x/b = 150$

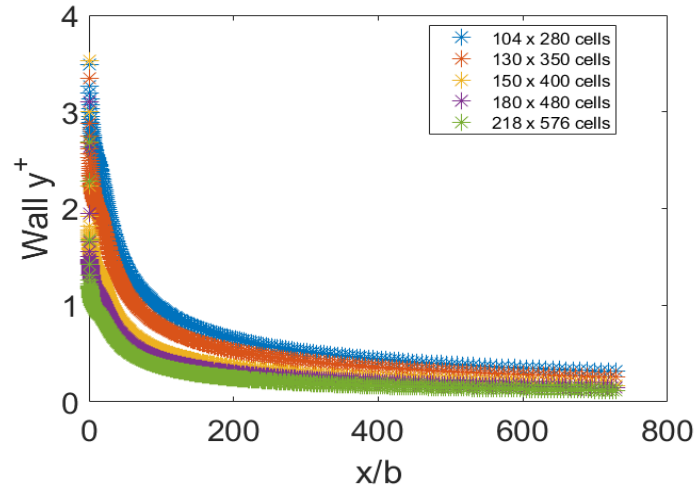


Figure 3.4 Comparison of wall y^+ for different meshes.

Since the profiles of velocity, TKE, and wall y^+ do not significantly change when refined above 150 x 400 cells, it indicates that grid independence has been attained. It was concluded from the grid study that the 150 x 400 cells mesh would be suitable as it is fine enough to capture the profiles with decent accuracy and is relatively quick to solve compared to more refined meshes. The 2D computational domain consisted of 60000 cells, as shown in Figure 3.5.

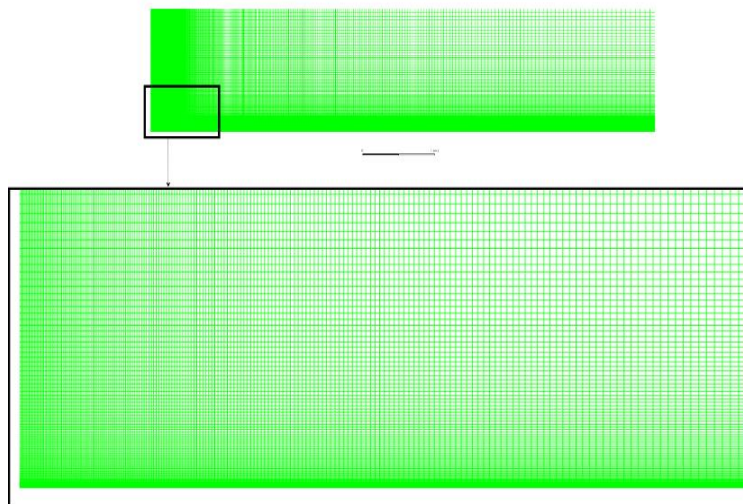


Figure 3.5 Computational domain generated in ANSYS meshing

4. RESULTS AND DISCUSSION

4.1 Quantities in inner scaling

4.1.1 Streamwise mean velocity in inner scaling

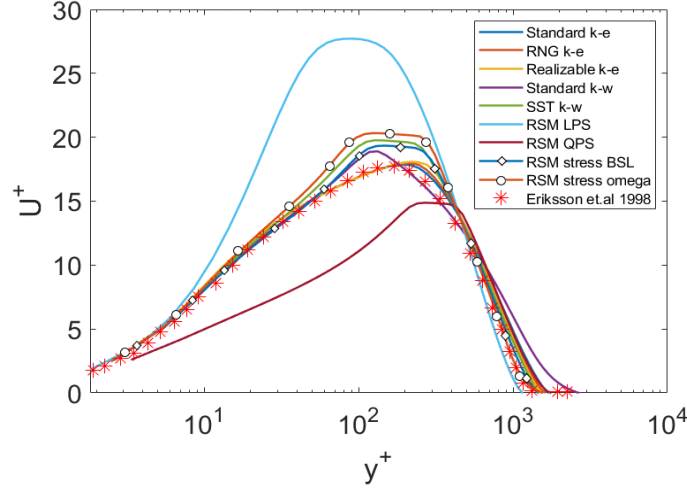


Figure 4.1 Streamwise mean velocity profile in inner scaling at $x/b = 10$

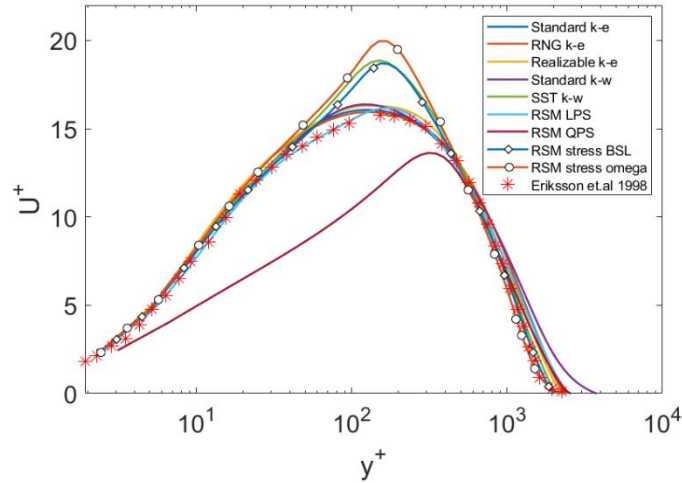


Figure 4.2 Streamwise mean velocity profile in inner scaling at $x/b = 20$

Figures 4.1, 4.2, and 4.3 illustrate, respectively, the profiles of streamwise mean velocity U in inner scaling at $x/b = 10, 20$ and 40 predicted by the chosen turbulence models at Reynolds number $Re = 9600$. A logarithmic scale was employed for values on the x -axis and for values on the y -axis, a linear one. Streamwise velocity U was normalised using friction velocity U_τ and y^+ is the non-dimensional distance from the wall surface. The standard $k - \varepsilon$, RNG $k - \varepsilon$, and realizable $k - \varepsilon$ all agree well with the experimental

results at $x/b = 10$. In the range of $35 < y^+ < 400$, the SST $k - \omega$, RSM stress BSL and RSM stress omega overestimate streamwise mean velocity U . This discrepancy is similar to that reported by Dejoan and Leschziner (2005), where the LES method could not replicate in the outer shear layer to boundary transition at $x/b = 10$ and 20. In the range $60 < y^+ < 170$, the standard $k - \omega$ shows a minor difference from the experimental results at $x/b = 10$. The RSM LPS and RSM QPS velocity profiles deviate significantly from the experimental values. The variation in wall shear stress at the inlet location shown in Figures 4.4(a) and 4.4(b) may explain this abnormal result.

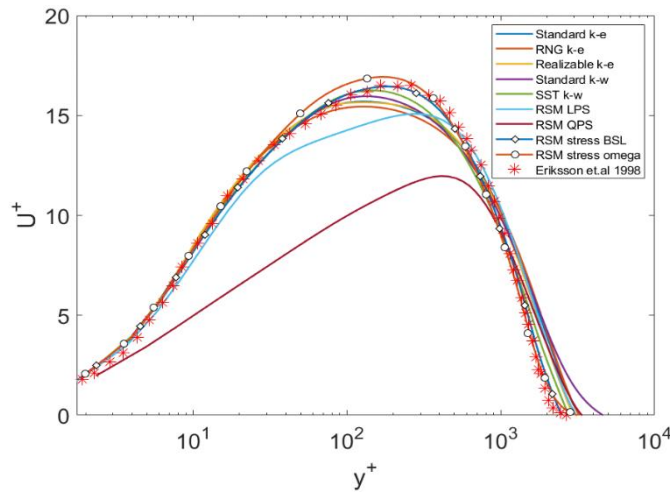


Figure 4.3 Streamwise mean velocity profile in inner scaling at $x/b = 40$

A comparison of Figures 4.1 and 4.2 reveals a definite decrease in the maximum value of U^+ for the SST $k - \omega$, RSM LPS, RSM stress BSL, and RSM stress omega as one moves downstream. At $x/b = 20$, three models—SST $k - \omega$, RSM stress BSL, and RSM stress omega deviate away from experimental data between $35 < y^+ < 400$, and all other models predict velocity well. This decrease in maximum value of U^+ shows the flow being developed. Moreover, RSM LPS agrees with the experimental data the best among all the turbulence models.

All models, except for the RSM QPS, match the experimental findings for velocity profiles at $x/b = 40$, which is presented in Figure 4.3. However, there is a slight deviation from the experiment for the RSM LPS between $30 < y^+ < 300$. This deviation could be

because wall shear stress was incorrectly predicted. A similar remark could be made about the RSM QPS. Overall, the flow transitioning from a laminar to a turbulent boundary layer between $x/b = 10$ and $x/b = 40$, is as expected by Eriksson et al. (1998). One can see a complete shift to a fully turbulent boundary layer by comparing Figures 4.2 and 4.3. The maximum value of U^+ was obtained around $y^+ = 200$ at $x/b = 40$. Furthermore, the RSM stress BSL and RSM stress omega show an excellent correlation with the experimental data at $x/b = 40$.

From Figure 4.4(b), we can observe that the RSM LPS predicts a laminar boundary layer up until about $x/b = 15$, at which point a sudden increase in wall shear stress is seen, indicating a change from a laminar to a turbulent boundary layer. This transition can be verified in Figure 4.2, which shows that RSM LPS and experimental data agree well. However, the RSM QPS predicts an early transition to a turbulent boundary layer and estimates higher wall shear stress than all other models. In summary, the wall shear stress predicted by the turbulence models may be causing the initial flow development to differ from experimental results. RSM QPS predicted around 40% higher wall shear stress at $x/b = 20$.

Figure 4.5(a) displays the wall y^+ for each turbulence model along the domain length, and Figure 4.5(b) displays the wall y^+ closer to the inlet region. The fact that y^+ along the wall was less than 1, suggesting that there were relatively small cells to capture velocity gradients effectively.

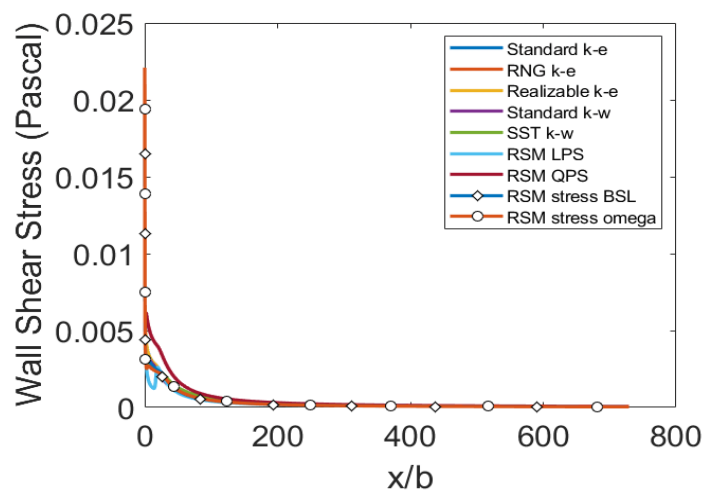


Figure 4.4(a) Wall shear stress comparison.

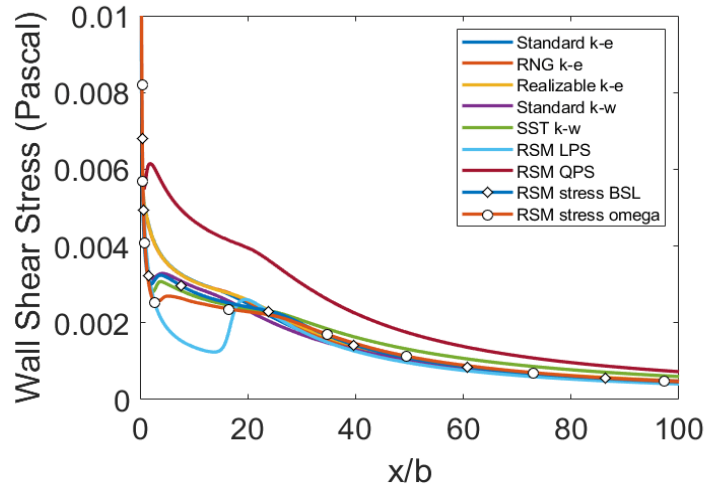


Figure 4.4(b) Wall shear stress in the inlet region

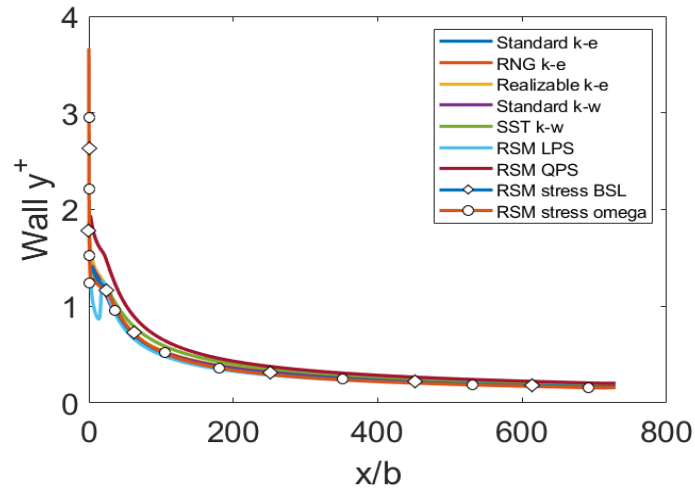


Figure 4.5(a) Wall y^+ comparison.

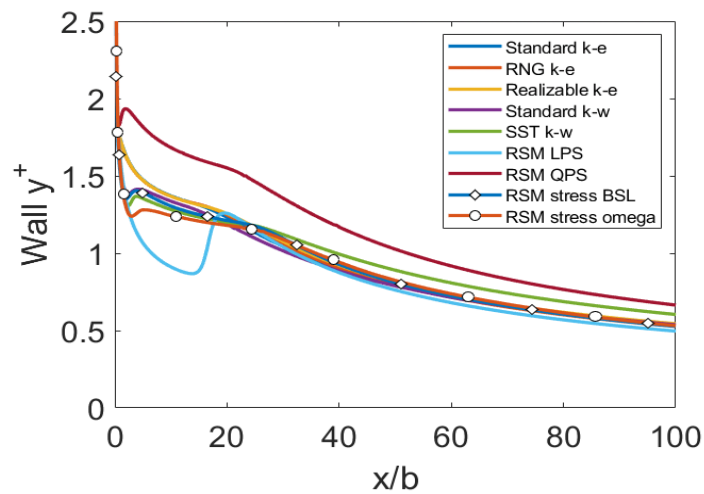


Figure 4.5(b) Wall y^+ in the inlet region.

Case	U_τ / U_0	y_m^+
Eriksson et al. (1998)	0.0524	167
Standard $k - \varepsilon$	0.0556	195
RNG $k - \varepsilon$	0.0554	218
realizable $k - \varepsilon$	0.0555	218
Standard $k - \omega$	0.0542	133
SST $k - \omega$	0.0520	127
RSM LPS	0.0370	90
RSM QPS	0.0682	269
RSM stress BSL	0.0529	146
RSM stress omega	0.0504	123

Table 1. Comparison between the turbulence model predicted and the experimental values of normalised friction velocity and maximum streamwise mean velocity location at $x/b = 10$

Table 1 compares the values of friction velocity at $x/b = 10$ normalised with mean inlet velocity from RANS models and the same from the experiment. Table 1 also gives the location of the local maximum streamwise velocity U_{max} in a non-dimensional form y_m^+ . The RSM QPS and RSM LPS produced anomalous results. The RSM LPS predicted U_τ / U_0 around 30% lower than the experiment, while RSM QPS is around 30% higher than the experiment. The predictions of U_τ / U_0 by all other turbulence models were within 6% of the experiment. The SST $k - \omega$ and RSM stress BSL were more accurate than other models as they were within 1% of the experiment. Looking at the y_m^+ values, one could see that the standard $k - \varepsilon$ and RSM stress BSL predicts more accurate values than other models, but these models were around 15% higher and lower than the experimental data, respectively.

Turning attention to the downstream, fully developed region of the jet, the inner scaled streamwise mean velocity profiles at $x/b = 70, 100$ and 150 are shown in Figures 4.6, 4.7 and 4.8, respectively. As previously mentioned, compared to other turbulence models, the RSM LPS and RSM QPS produced abnormal results that may be connected to a larger estimate of wall shear stress. All the other models agree with experimental data between $1 < y^+ < 100$ at $x/b = 70, 100$ and 150 . Above $y^+ > 100$, the numerical models deviate slightly from the experimental data.

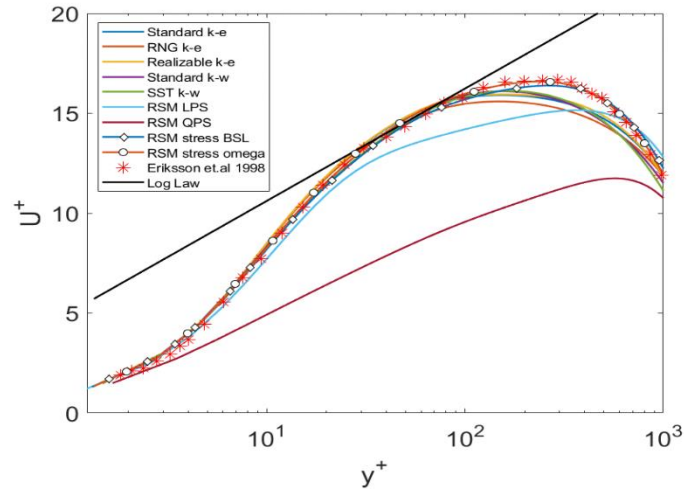


Figure 4.6 Streamwise mean velocity profile in inner scaling at $x/b = 70$

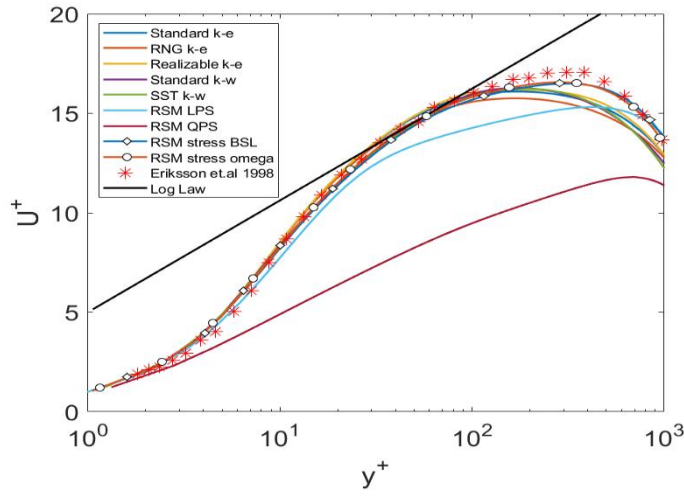


Figure 4.7 Streamwise mean velocity profile in inner scaling at $x/b = 100$

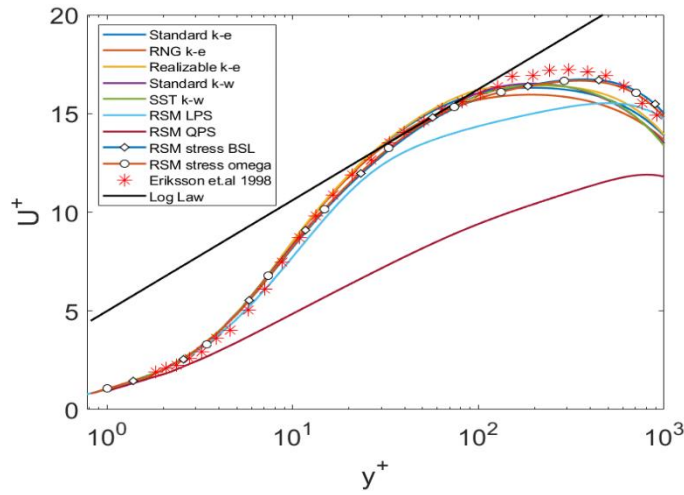


Figure 4.8 Streamwise mean velocity profile in inner scaling at $x/b = 150$

The RSM stress omega and RSM stress BSL matched the experimental data better than other turbulence models where $y^+ > 100$ at $x/b = 70, 100$ and 150 . Also, the $k - \varepsilon$ and $k - \omega$ models predicted lower mean velocity values than the experimental data at all locations in the fully developed region. Inaccurate Reynolds shear stress predictions in the outermost region of the flow could account for this difference. On the figures, the line depicting the relation $U^+ = 2.44 \ln y^+ + 5.0$ has also been drawn. In general, this equation holds for boundary layers on flat plates. Furthermore, the maximum value of U^+ was obtained around $y^+ = 250$ at $x/b = 150$

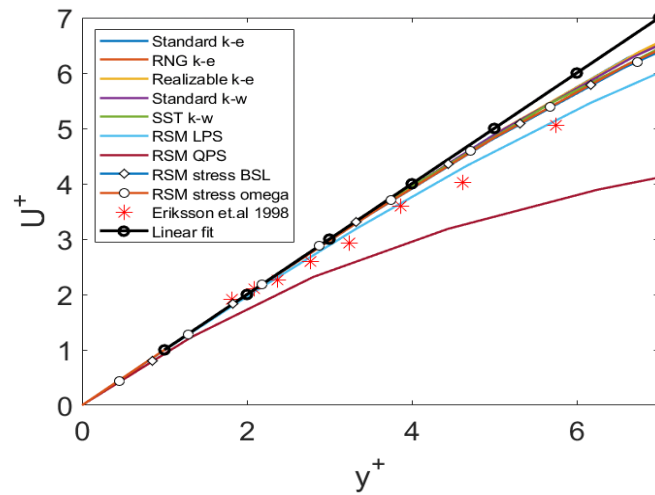


Figure 4.9 Streamwise mean velocity profile in near wall region at $x/b = 100$

The very near-wall region of the streamwise velocity profile at $x/b = 100$ along with a linear velocity profile, is shown in Figure 4.9. The RSM LPS generates a profile that is identical to the experiment in this region until y^+ around 7. Up until $y^+ = 3$ to 4, the linear velocity profile is consistent with the profiles generated by turbulence models (except for RSM QPS), but after that, the models diverge. A similar observation was made by Dejoan and Leschziner (2005). On the other hand, the two-equation models, RSM stress BSL and RSM stress omega are closely in agreement with the linear profile.

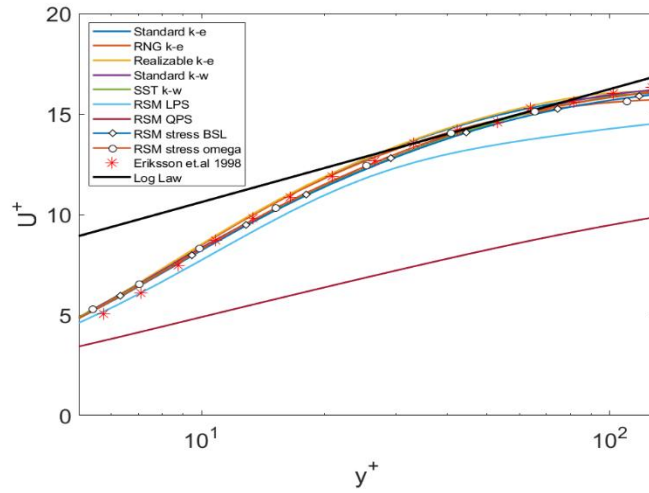


Figure 4.10 Streamwise mean velocity profile in inner scaling at $x/b = 100$

Figure 4.10 shows a zoomed view of the streamwise mean velocity profile at $x/b = 100$ in the near wall region. The log law line and numerical data are in agreement for a brief period between $20 < y^+ < 80$ at $x/b = 100$. However, a line with a different slope would match the profiles better.

4.1.2 Turbulent kinetic energy (TKE) in inner scaling

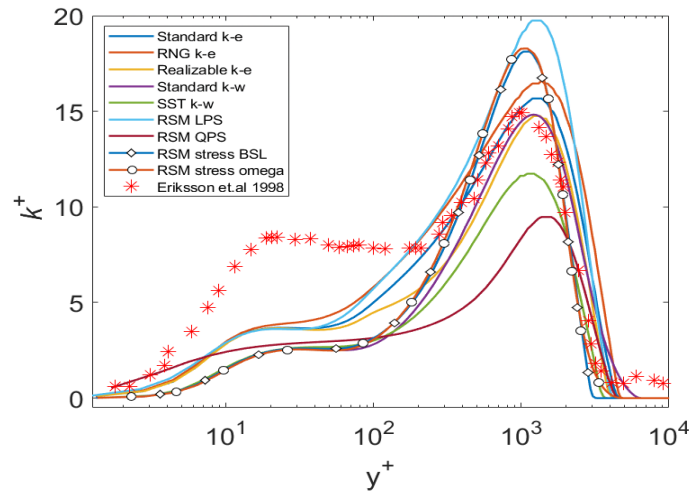


Figure 4.11 TKE profile in inner scaling at $x/b = 70$

Figure 4.11 provides the TKE profile scaled with inner variables at $x/b = 70$. The experimental data were obtained from Dejoan and Leschziner (2005), based on the data by Eriksson et al. (1998). The overall profiles from numerical modelling are similar to the

experiment. However, there is a mismatch in the inner layer where $y^+ < 200$. A possible reason for this difference could be the Boussinesq approximation, which assumes all the normal Reynolds stresses are equal in value. The location of the inner peak is around $y^+ = 20$, and the outer peak is around $y^+ = 1050$ in all cases. The inner peak value from numerical results is at least 57% lower than the experiment, which is quite a significant difference. Beyond $y^+ = 200$, numerical results and experimental data match better. The standard $k - \varepsilon$, realizable $k - \varepsilon$ and standard $k - \omega$ match the experiment well. The Reynolds stress models predict about 18% higher TKE values than experimental data in the outer layer. Both in numerical results and the experiment, a plateau can be seen. It is between $20 < y^+ < 200$ in the experiment, whereas in the computed values, it is between $14 < y^+ < 70$.

4.1.3 Reynolds shear stress in inner scaling

The Reynolds shear stress profiles in inner scaling for $x/b = 10, 20$ and 40 are shown in Figures 4.12, 4.13 and 4.14. Reynolds shear stress was normalised using U_τ^2 where U_τ is friction velocity. A common observation from the figures for Reynolds stress profiles is the two peaks – inner and outer peak. Also, the profiles are similar in shape compared to experimental data.

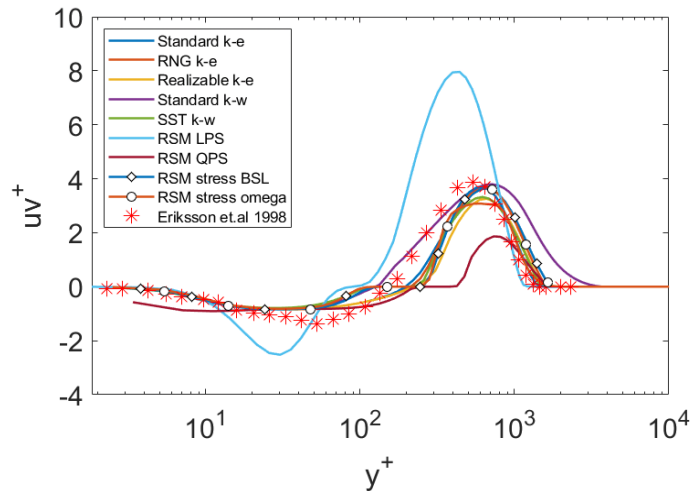


Figure 4.12 Reynolds shear stress profile in inner scaling at $x/b = 10$

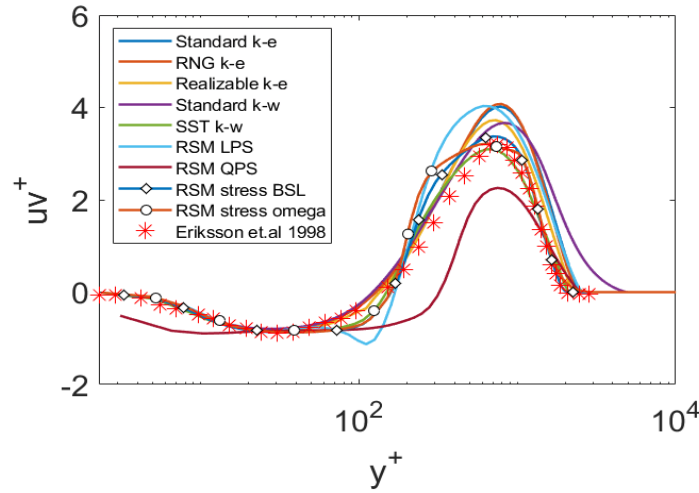


Figure 4.13 Reynolds shear stress profile in inner scaling at $x/b = 20$

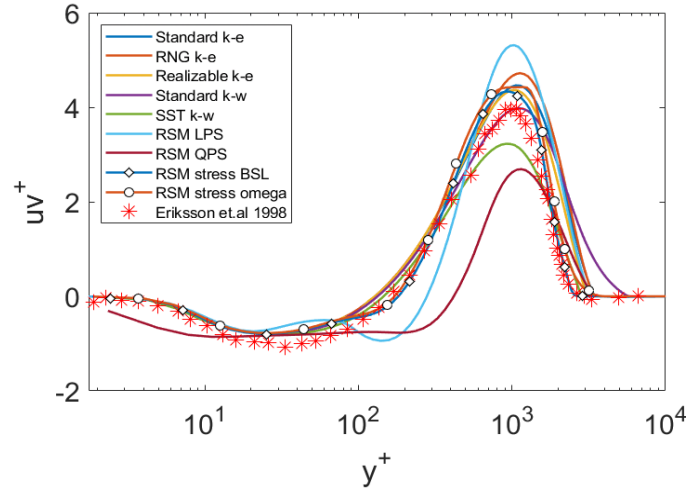


Figure 4.14 Reynolds shear stress profile in inner scaling at $x/b = 40$

All models, except RSM LPS and RSM QPS, can reasonably estimate Reynolds shear stress at $x/b = 10$. Reynolds shear stress profiles from RSM QPS are 50% lower than the experiment, whereas it is around 50% higher for RSM LPS. A possible reason for such deviation in normalised Reynolds shear stress could be the wall shear stress predicted by turbulence models near to jet inlet. This discrepancy could explain why the velocity profiles produced by RSM LPS and RSM QPS initially deviate further than other turbulence models from experimental data.

Furthermore, one can see an increase in the negative inner peak from $x/b = 10$ to 40. The Reynolds shear stress at $x/b = 40$ has an outer positive peak of 4 around $y^+ = 1000$ and a negative inner peak value of -1 around $y^+ = 30$. According to Eriksson et al. (1998), this indicates the development of the inner layer into a turbulent boundary layer with zero pressure gradient. The velocity gradients between the boundary layer and the wall could be the reason for the inner peak, whereas the velocity gradients created between the high velocity fluid and the ambient flow could be the reason for the outer peak in the Reynolds shear stress profiles. These two peaks provide evidence of two locations where turbulence is produced.

At $x/b = 20$, SST $k - \omega$ and RSM stress BSL coincide with experimental measurements excellently. However, at $x/b = 40$, SST $k - \omega$ deviates between $600 < y^+ < 1050$ by 25%. All the models except RSM LPS and RSM QPS match quite well between $0 < y^+ < 600$ at $x/b = 40$. In Figure 4.14, when $y^+ > 1050$, RSM stress BSL and RSM stress omega best match the experiment. Reynolds shear stress is close to zero at two locations – in the viscous sublayer and around $y^+ = 100$. These are the locations where velocity gradients are minimal. The magnitude of Reynolds shear stress is equal to U_τ^2 around $y^+ = 200$.

4.2 Quantities in outer scaling

4.2.1 Streamwise mean velocity in outer scaling

Figures 4.15 to 4.18 depict the streamwise mean velocity profiles in outer scaling using the RANS models, and profiles are compared to experimental data wherever possible. U_{max} was used to normalise the velocity U , while $y_{1/2}$ was used to normalise the wall distance y . At $x/b = 10$, all the models except the standard $k - \omega$ model and RSM QPS have a similar profile. This discrepancy in velocity profiles predicted by the standard $k - \omega$ model and RSM QPS could be due to flow transitioning from laminar to turbulent. In the inner region $y/y_{1/2} < 1$, all models except RSM QPS have the same profile and agree with the experimental data at $x/b = 20$. The two-equation $k - \varepsilon$ models agree with the experiment better in the inner region at $x/b = 20$.

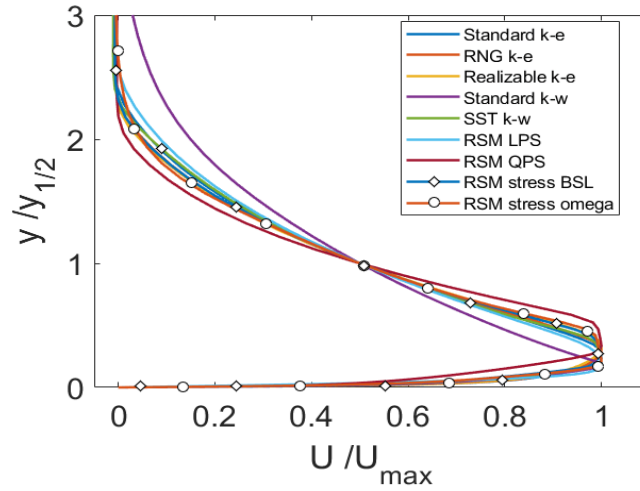


Figure 4.15 Streamwise mean velocity profile in outer scaling at $x/b = 10$

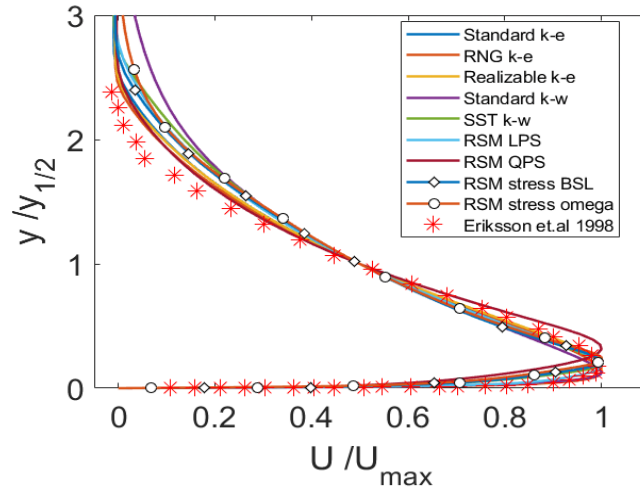


Figure 4.16 Streamwise mean velocity profile in outer scaling at $x/b = 20$

Again, except for the RSM QPS, the velocity profiles match each other well at $x/b = 30$ where the flow is still developing. The numerical and experimental results agree well at $x/b = 40$, indicating a well-developed boundary layer. There is, however, a discrepancy between turbulence models and experimental data at the outermost portion of the profiles at all streamwise positions where $y/y_{1/2} > 1$ which may be caused by mixing between layers. At $x/b = 40$, RSM LPS, RSM stress BSL and RSM stress omega give the best match with the experiment along the entire profile. However, the $k - \varepsilon$ models are not too far. Although not very significant, the family of $k - \varepsilon$ and $k - \omega$ produced a higher

streamwise velocity in the outer region where $y/y_{1/2} > 1$ compared to the experiment and the Reynolds stress model variants.

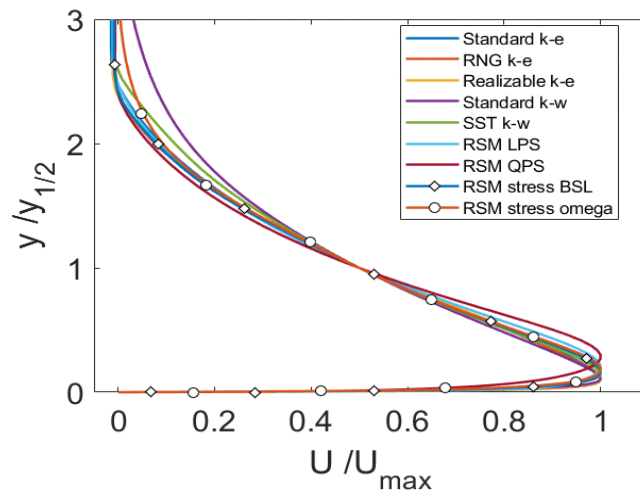


Figure 4.17 Streamwise mean velocity profile in outer scaling at $x/b = 30$

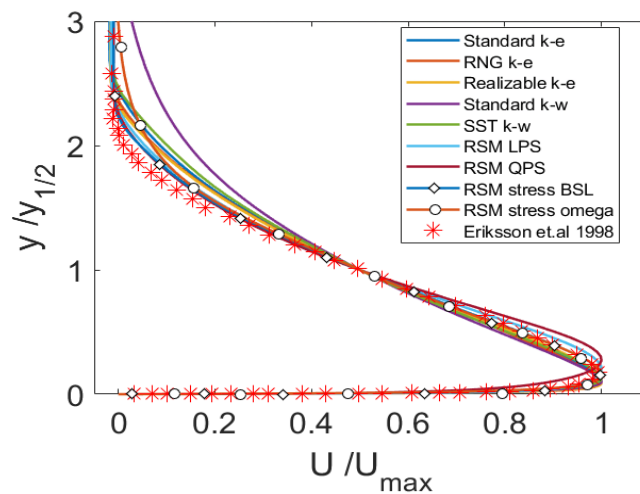


Figure 4.18 Streamwise mean velocity profile in outer scaling at $x/b = 40$

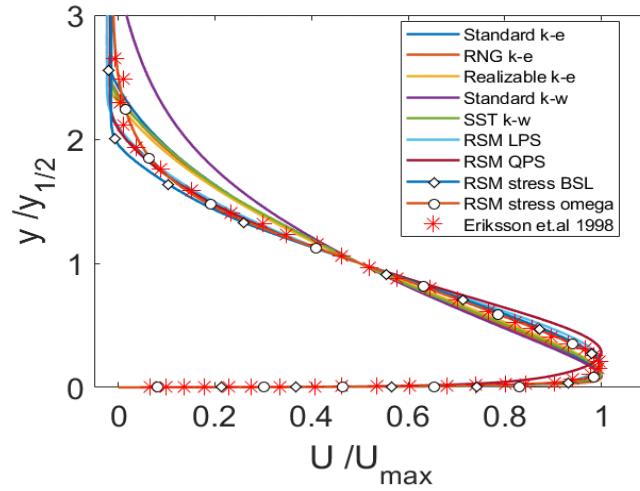


Figure 4.19 Streamwise mean velocity profile in outer scaling at $x/b = 70$

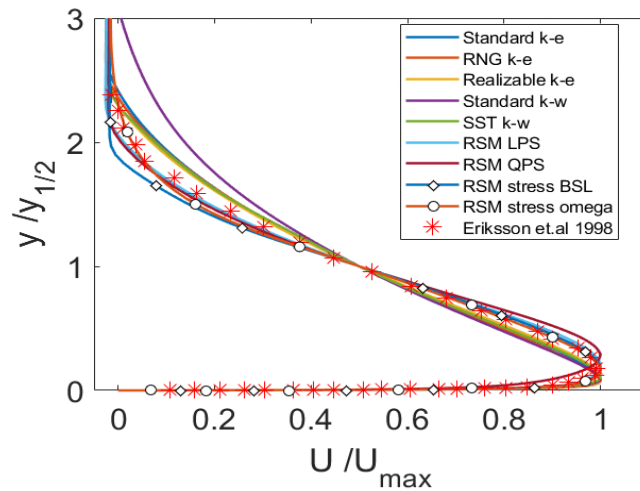


Figure 4.20 Streamwise mean velocity profile in outer scaling at $x/b = 100$

Figures 4.19 to 4.22 show the streamwise mean velocity profiles in outer scaling in the downstream, fully developed region. The velocity profiles match well with experimental data at all locations when $y/y_{1/2} < 1$ and the only exception is the RSM QPS, which departs slightly from the data. At $x/b = 70$ and 100 , RSM LPS, RSM stress BSL and RSM stress omega coincide excellently with experimental data in the inner and outer regions.

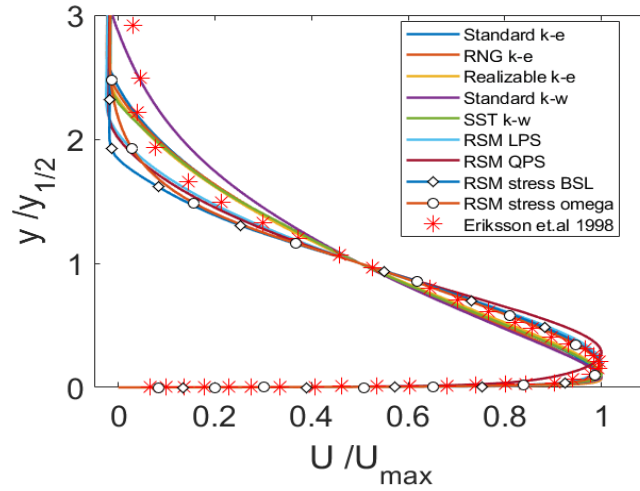


Figure 4.21 Streamwise mean velocity profile in outer scaling at $x/b = 150$

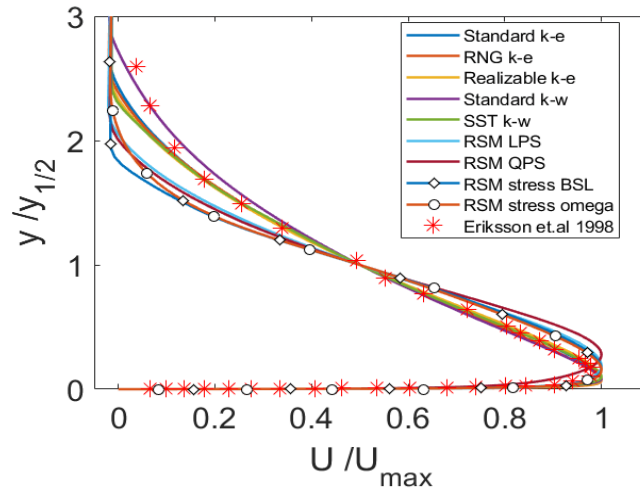


Figure 4.22 Streamwise mean velocity profile in outer scaling at $x/b = 200$

RSM LPS, RSM stress BSL, and RSM stress omega underpredict the mean velocity profile in the outer region where $y/y_{1/2} > 1$ and overpredict profile in the inner region where $y/y_{1/2} < 1$ at $x/b = 150$ and 200 . This inconsistency may be because of the location of maximum velocity or perhaps the maximum velocity U_{max} was wrongly estimated. The standard $k - \varepsilon$, RNG $k - \varepsilon$, and realizable $k - \varepsilon$ all suit the experimental data better when $x/b = 200$. It is noteworthy to observe that all of the variations within each family of turbulence models— $k - \varepsilon$, $k - \omega$ and RSM—produce identical profiles.

4.2.2 Growth rate of the wall jet

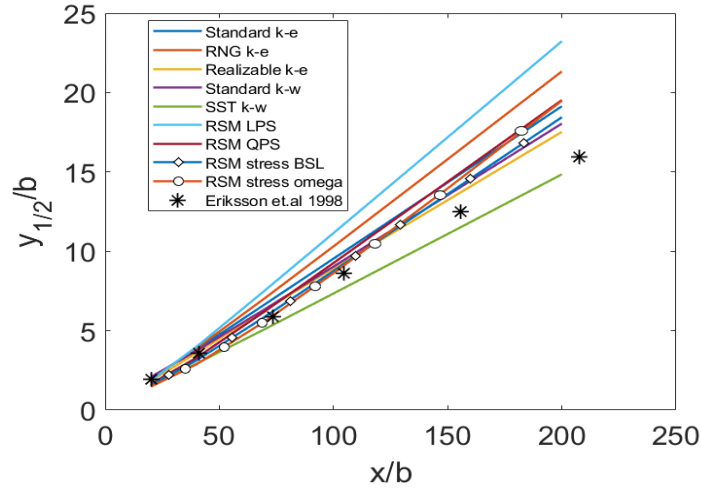


Figure 4.23 Jet growth rate along the streamwise direction

The jet's half-height growth rate along the wall is depicted in a dimensionless form in Figure 4.23. Up to approximately $x/b = 40$, the jet growth rate of all models can be shown to follow the same slope. This observation is consistent with the experiment's findings and suggests that all models predicted flows with a similar jet growth rate in the jet's initial development region. The jet growth rates begin to diverge after $x/b = 40$, and the differences in the results are wider as one proceeds along the wall away from the inlet. Overprediction of Reynolds shear stress by the turbulence models in the fully developed region could be a possible reason for this deviation.

The SST $k - \omega$ and realizable $k - \varepsilon$ models closely match the experimental data. In contrast to all other models, the SST $k - \omega$ model consistently underestimates the growth rate in the developed region. Up to about $x/b = 80$, the variation in jet half width predicted by the RSM stress omega model is nearly identical to the experiment but overpredicts it further downstream. Regarding jet growth rate, the RSM LPS and RNG $k - \varepsilon$ are the least accurate.

A linear relation of the form $y_{1/2}/b = A(x/b) + B$ was assumed, where A and B are constants and such a linear line was fitted in the numerical data for each turbulence model using Microsoft Excel. The constants A and B thus found are given in Table 2. The

constant A is the resulting streamwise rate of spread $dy_{1/2}/dx$, which is around 0.0782, according to Eriksson et al. (1998). The spread rate for SST $k - \omega$ is 0.0739, which lies in the range 0.073 ± 0.002 given by Launder and Rodi (1981). This value predicted SST $k - \omega$ model was about 5.5% lower than the experiment by Eriksson et al. The following best turbulence model was the realizable $k - \varepsilon$, which is 11.5% higher than the experiment. All the other turbulence models predict a significantly higher spread rate than the experiment.

Case	Constant A	Constant B
Eriksson et al. (1998)	0.0782	0.332
Standard $k - \varepsilon$	0.0955	0.0201
RNG $k - \varepsilon$	0.108	-0.3794
realizable $k - \varepsilon$	0.0872	0.1473
Standard $k - \omega$	0.089	0.1994
SST $k - \omega$	0.0739	0.0062
RSM LPS	0.1194	-0.7112
RSM QPS	0.1002	-0.6213
RSM stress BSL	0.0945	-0.5664
RSM stress omega	0.1012	-1.1142

Table 2. Comparison of streamwise rate of the spread between $x/b = 20$ and $x/b = 200$

4.2.3 Decay of streamwise mean velocity

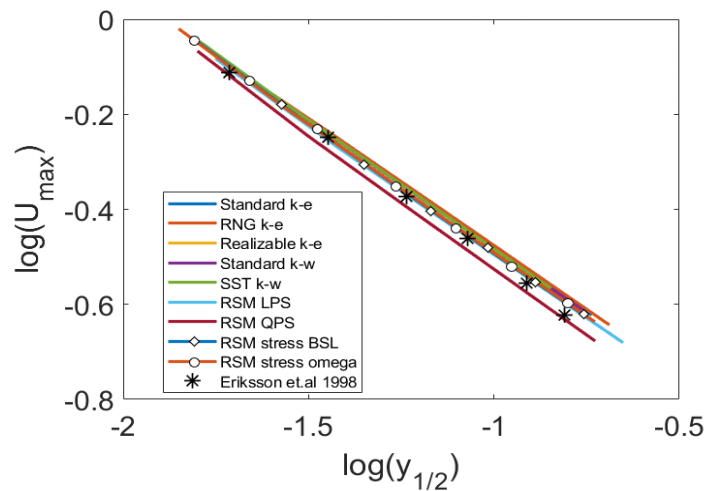


Figure 4.24 Maximum streamwise mean velocity decay

In a log-log plot, Figure 4.24 depicts the decrease of the maximum streamwise mean velocity at streamwise locations as a function of jet half width. All of the models and the experimental data compare favourably quite well; however, there is a minor deviation as one moves downstream from the jet inlet. For the RSM QPS, the line is slightly off by a small margin relative to other models but maintains a similar slope.

4.2.4 Turbulent kinetic energy (TKE) in outer scaling

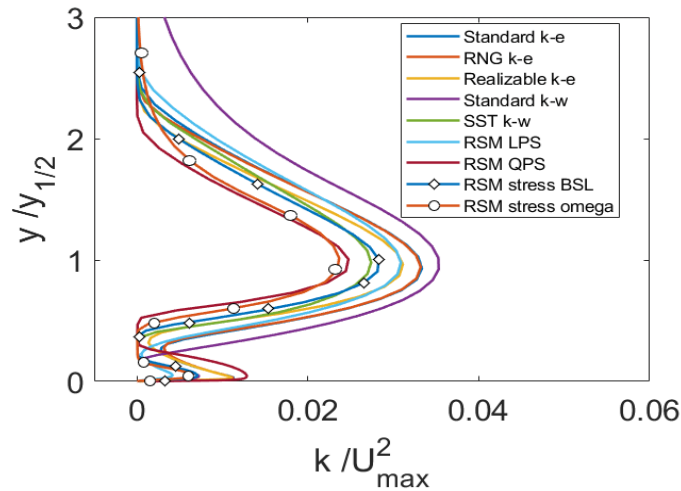


Figure 4.25 TKE profile in outer scaling at $x/b = 10$

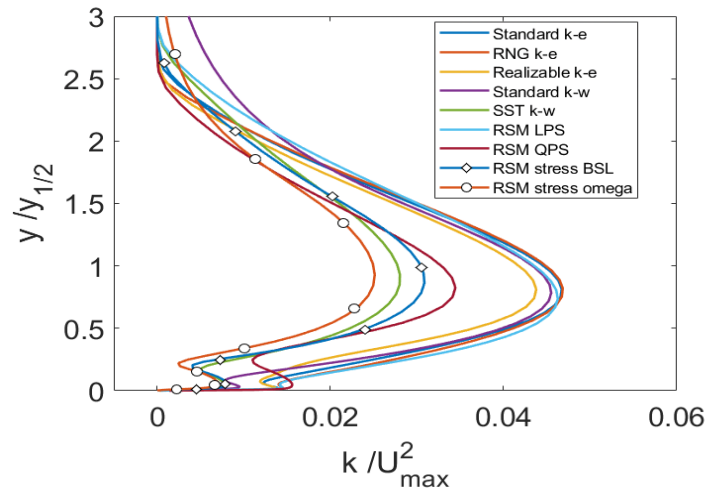


Figure 4.26 TKE profile in outer scaling at $x/b = 20$

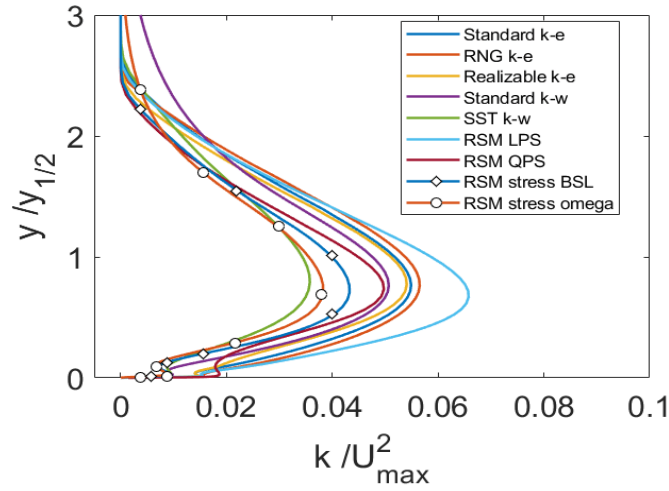


Figure 4.27 TKE profile in outer scaling at $x/b = 30$

Figures 4.25 to 4.28 present profiles of TKE in the outer scaling at, correspondingly, $x/b = 10, 20, 30$ and 40 . U_{max}^2 was used to normalise TKE k . The profiles clearly show two peaks—an inner peak and an outer peak—at each location. The inner peak is near the wall, whereas the outside peak is near $y/y_{1/2} = 1$.

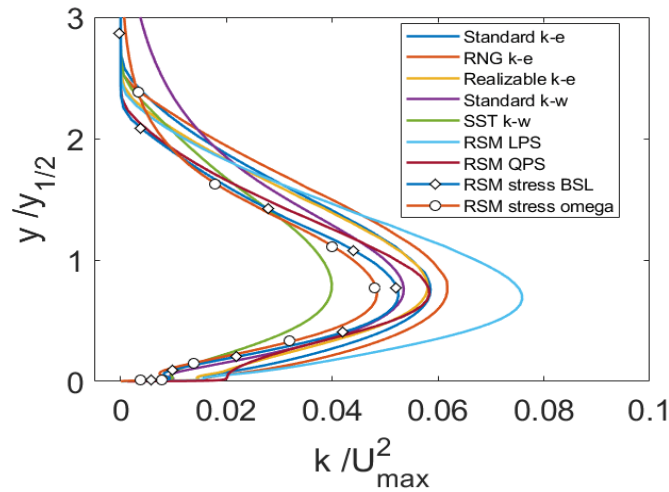


Figure 4.28 TKE profile in outer scaling at $x/b = 40$

Between $x/b = 10$ and $x/b = 40$, the values of normalised TKE in the inner and outer regions vary. The two peaks are distinctly apparent at $x/b = 10$, and as one goes

downstream, the value of the outer peak rises. This increase in value is another example of how the flow has evolved. The flow becomes more turbulent as one moves away from the jet inlet, and finally, the jet loses strength as energy dissipates. The more prominent outer peak shows that the region between the high velocity fluid and the ambient generates more turbulence than the inner layer.

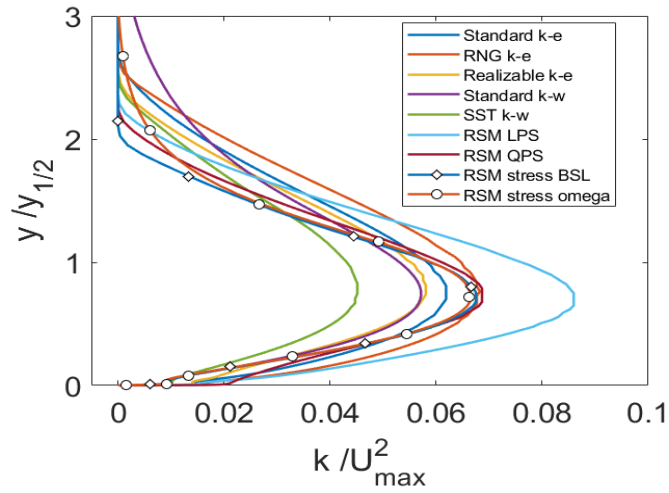


Figure 4.29 TKE profile in outer scaling at $x/b = 70$

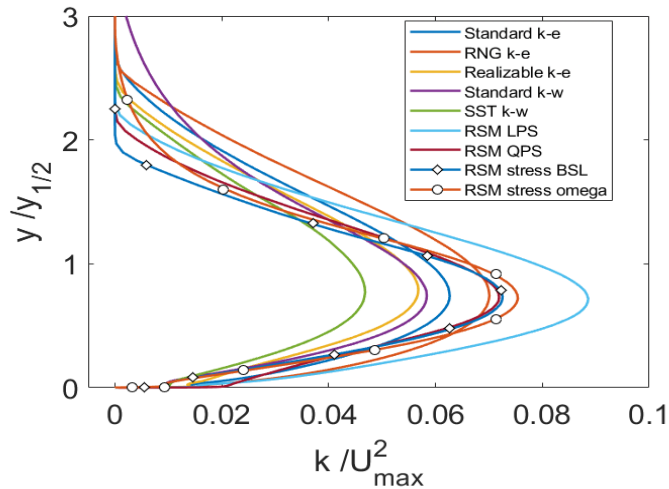


Figure 4.30 TKE profile in outer scaling at $x/b = 100$

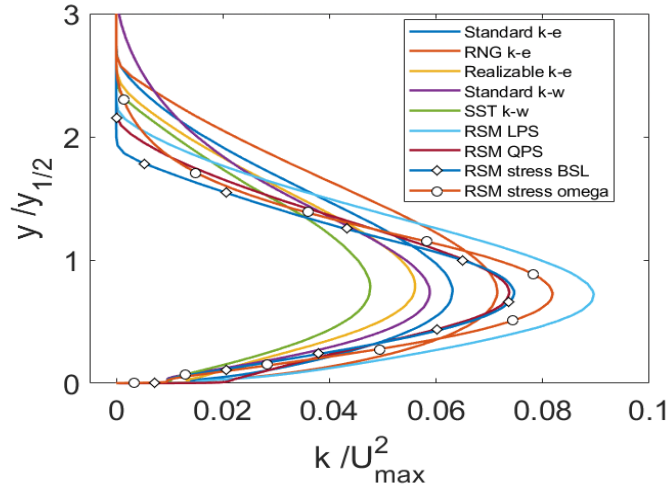


Figure 4.31 TKE profile in outer scaling at $x/b = 150$

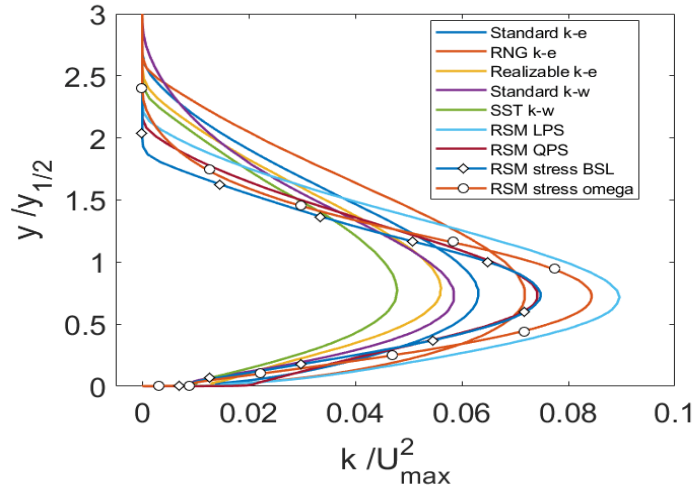


Figure 4.32 TKE profile in outer scaling at $x/b = 200$

The TKE profiles in the downstream, fully developed region are discussed next. The TKE profiles are normalised with U_{max}^2 in the fully developed region from $x/b = 70$ to 200, as shown in Figures 4.29 to 4.32. From $x/b = 70$ and downstream, the peak values of TKE rise with streamwise position, although much less than seen in the early jet development. Moreover, the inner peak is almost nonexistent in the fully developed region. The SST $k - \omega$ predicts the lowest levels of turbulence and RSM LPS the highest in every case. The general form of all the profiles is the same. The two-equation models predict lower outer peak values than the experiment, and the TKE profiles range from $0 < y/y_{1/2} < 2.5$.

The Reynolds stress models indicate higher outer peak values for TKE than the experiment and range from $0 < y/y_{1/2} < 2$. In short, two-equation models produce broader profiles with lower peaks relative to Reynolds stress models.

4.2.5 Reynolds shear stress in outer scaling

Outer scaled Reynolds shear stress profiles in the downstream, fully developed region are shown in Figures 4.33, 4.34 and 4.35. They depict the variations in the Reynolds shear stress normalised with U_{max}^2 profiles at, respectively, $x/b = 70, 100$ and 150 . All the models except RSM LPS and RSM QPS agree well with experimental results close to the wall up to around $y/y_{1/2} = 0.25$ at $x/b = 70, 100$ and 150 . But none of the models predicted the negative inner peak accurately. Only the SST $k - \omega$ matches with the experimental data closely between $0.25 < y/y_{1/2} < 1.5$ even though it predicts lower values than the experiment in the fully developed region. Every other model generates results with outer peak values 1.5 to 3 times higher than the experimental data.

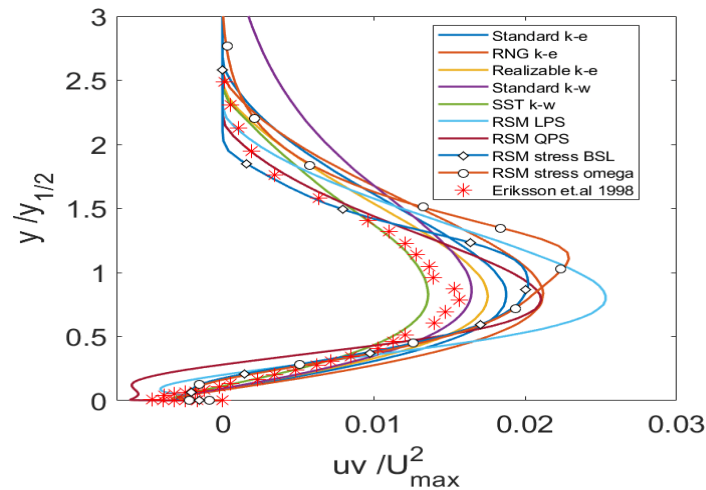


Figure 4.33 Reynolds shear stress profile in outer scaling at $x/b = 70$

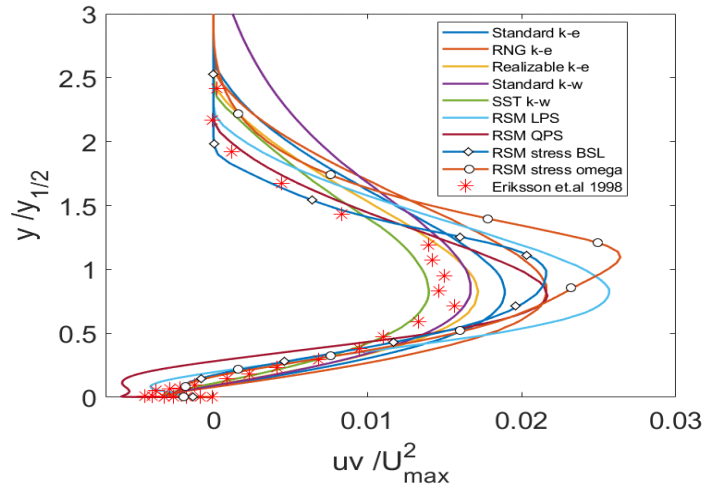


Figure 4.34 Reynolds shear stress profile in outer scaling at $x/b = 100$

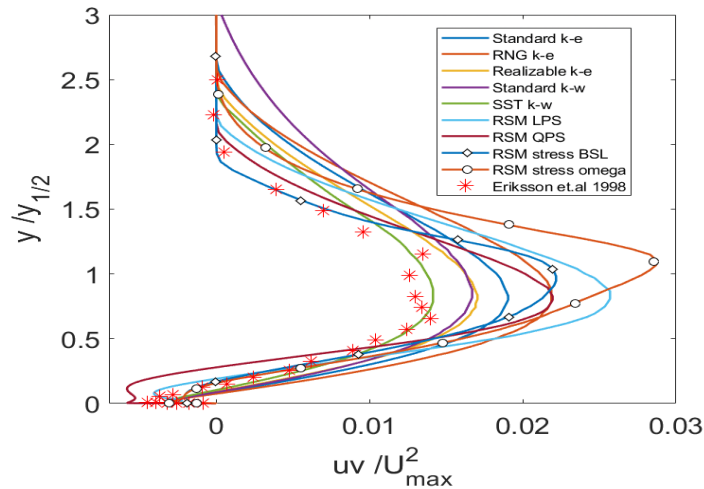


Figure 4.35 Reynolds shear stress profile in outer scaling at $x/b = 150$

The RSM stress BSL closely resembles the experimental data above $y/y_{1/2} = 1.5$ at all locations selected in the developed region. The realizable $k - \varepsilon$ model yield results that are satisfactory across the entire profile. From $x/b = 70$ downstream, the profiles generated by each model do not appear to differ significantly. However, an intriguing finding is that, compared to the more complicated Reynolds stress model, two-equation models based on the Boussinesq hypothesis generate significantly more accurate flow features in some cases.

CONCLUSION

A two-dimensional turbulent wall jet in quiescent surroundings at a Reynolds number of 9600 based on a jet inlet height of 9.6mm was modelled using various RANS turbulence models available in the commercial software ANSYS Fluent. The objective was to identify the most suitable RANS model to model the wall jet. A pressure-based, steady, incompressible double precision solver was used, with spatial discretisation being second-order accurate. Numerical results produced by the standard $k - \varepsilon$, RNG $k - \varepsilon$, realizable $k - \varepsilon$, standard $k - \omega$, SST $k - \omega$, RSM LPS, RSM QPS, RSM stress BSL and RSM stress omega were compared with experimental results of Eriksson et al. (1998). All the simulations were run with the enhanced wall treatment option enabled. In addition, the computational domain and boundary conditions were selected to mimic the experimental setup.

Initially, a grid independence study was performed to obtain the most suitable mesh using the standard $k - \varepsilon$ model. This optimal mesh was used for further simulations and analysis. A scaled residual of 1×10^{-5} was achieved for all the transport equations. Streamwise velocity profiles, turbulence quantities such as turbulent kinetic energy and Reynolds shear stress in inner and outer scaling at various streamwise locations were plotted. Profiles of various quantities at $x/b = 10, 20, 30, 40, 70, 100, 150$ and 200 , where b is the jet inlet height, were studied.

We can conclude from the profiles that different turbulence models perform better under certain conditions. In the developing region, the standard $k - \varepsilon$, RNG $k - \varepsilon$ and realizable $k - \varepsilon$ were able to produce streamwise velocity profiles similar to the experiment. The maximum velocity was achieved around $y^+ = 250$. The velocity profiles scaled with inner variables coincided with the log law line between $20 < y^+ < 80$. However, the numerical models were not able to predict velocity well in the outer layer $y/y_{1/2} > 1$. The value of normalised friction velocity U_τ / U_0 predicted by the SST $k - \omega$ and RSM stress BSL were more accurate than other models. Additionally, the y_m^+ value was more accurately predicted by the standard $k - \varepsilon$ and RSM stress BSL than other models. The RSM stress

BSL and RSM stress omega produced more accurate Reynolds shear stress profiles compared to other turbulence models at streamwise locations $x/b = 10$ to 40 . The SST $k - \omega$ and realizable $k - \varepsilon$ models produced relatively more accurate jet growth rate along the wall, followed by RSM stress BSL and RSM stress omega. All models except RSM QPS predicted maximum streamwise velocity decay well.

In the developed region, RSM BSL and RSM stress omega produce streamwise velocity profiles better than other models. However, at $x/b = 200$, the velocity profile produced by the standard $k - \varepsilon$, RNG $k - \varepsilon$, and realizable $k - \varepsilon$ were better than other models. SST $k - \omega$ and realizable $k - \varepsilon$ produced a better match for Reynolds shear stresses in the developed region. Except for RSM QPS, all models predict near-wall mean velocity well. RSM LPS matches the experiment sufficiently, and other models are closer to the linear velocity profile. For turbulent kinetic energy profiles, SST $k - \omega$ produces the lowest value, and RSM LPS predicts the highest than the rest of the models. None of the RANS turbulence models was able to model the peak value of turbulent kinetic energy accurately at $x/b = 70$ in the inner region of the flow where $y^+ < 200$. The inner peak in TKE profiles was at around $y^+ = 20$.

Overall, RSM stress BSL is more favourable for modelling turbulent wall jets because it could reproduce velocity profiles, turbulent kinetic energy and Reynolds shear stress profiles with relatively good accuracy. Although the model's performance is not always the best, RSM stress BSL does not deviate from the experiment as much as the other models. The RSM stress omega could be considered as the following best.

The present work can be extended to investigate the fluid and thermal behaviour of the turbulence models using adiabatic and uniform heat flux conditions for the wall. The selected turbulence models could be tested at different inlet Reynolds numbers and compared with published experimental data to see how numerical models behave under different conditions. Also, the least accurate turbulence models in the present study can be eliminated, and newer models can be tested in the future. Furthermore, a 3D computational domain could be utilized to find the most suitable turbulence model for modelling a 3D wall jet.

REFERENCES

- Balabel, A. and El-Askary, W.A. (2011) “On the performance of linear and non-linear k - ϵ turbulence models in various jet flow applications,” *Eur. J. Mech. B Fluid* 30 325–340. doi:<https://doi.org/10.1016/j.euromechflu.2010.10.006>.
- Craft, T.J. and Launder, B.E. (2001) “On the spreading mechanism of the three-dimensional turbulent wall jet”, *Journal of Fluid Mechanics*, 435, pp. 305-326. doi: 10.1017/S0022112001003846.
- Dejoan, A., and Leschziner, M.A. (2005) “Large eddy simulation of a plane turbulent wall jet”, *Physics of Fluids*, 17(2), p. 025102. doi: 10.1063/1.1833413.
- Eriksson, J., Karlsson, R. and Persson, J. (1998) “An experimental study of a two-dimensional plane turbulent wall jet”, *Experiments in Fluids*, 25(1), pp. 50-60. doi: 10.1007/s003480050207.
- Fu, C., Uddin, M. and Curley, A. (2016) “Insights derived from CFD studies on the evolution of planar wall jets”, *Engineering Applications of Computational Fluid Mechanics*, 10:1, 44-56, doi: 10.1080/19942060.2015.1082505
- Kakka, P. and Anupindi, K. (2021) “Flow and thermal characteristics of three-dimensional turbulent wall jet”, *Physics of Fluids*, 33(2), p. 025108. doi: 10.1063/5.0031138.
- Kechiche, J., Mhiri, H., Palec, G.L., and Bournot, P. (2004) “Application of low Reynolds number k - ϵ turbulence models to the study of turbulent wall jets”. *International Journal of Thermal Sciences*, 43, 201-211. doi: 0.1016/j.ijthermalsci.2003.06.005
- Launder, B. and Rodi, W. (1981) “The turbulent wall jet”, *Progress in Aerospace Sciences*, 19, pp. 81-128. doi: 10.1016/0376-0421(79)90002-2.
- Launder, B. and Rodi, W. (1983) “The Turbulent Wall Jet Measurements and Modeling”, *Annual Review of Fluid Mechanics*, 15(1), pp. 429-459. doi: 10.1146/annurev.fl.15.010183.002241.
- Launder, B. and Sharma, B. (1974) “Application of the energy-dissipation model of turbulence to the calculation of flow near a spinning disc”, *Letters in Heat and Mass Transfer*, 1(2), pp. 131-137. doi: 10.1016/0094-4548(74)90150-7
- Launder, B.E. and Spalding, D.B. (1974) “The numerical computation of turbulent flows”, *Computer Methods in Applied Mechanics and Engineering*. 3 (2): 269–289. doi:10.1016/0045-7825(74)90029-2.
- Launder, B.E., Reece, G., and Rodi, W. (1975) “Progress in the development of a Reynolds-stress turbulence closure”, *Journal of Fluid Mechanics*, 68(3), 537-566. doi:10.1017/S0022112075001814
- Ljuboja, M. and Rodi, W. (1980) “Calculation of Turbulent Wall Jets With an Algebraic Reynolds Stress Model”, *Journal of Fluids Engineering*, 102(3), pp. 350-356. doi: 10.1115/1.3240693.
- M. E. Schneider and R. J. Goldstein. (1994) “Laser Doppler measurement of turbulence parameters in a two-dimensional plane wall jet,” *Phys. Fluids* 6(9), 3116
- Menter, F. R. (1994) “Two-Equation Eddy-Viscosity Turbulence Models for Engineering Applications,” *AIAA Journal*, Vol. 32, No. 8, pp. 1598–1605. doi:10.2514/3.12149

- Naqavi, I., Tyacke, J. and Tucker, P. (2018) "Direct numerical simulation of a wall jet: flow physics", *Journal of Fluid Mechanics*, 852, pp. 507-542. doi: 10.1017/jfm.2018.503.
- Newman, B., Patel, R., Savage, S., and Tjio, H. (1972) "Three-Dimensional Wall Jet Originating from a Circular Orifice". *Aeronautical Quarterly*, 23(3), 188-200. doi:10.1017/S0001925900006089
- Pelfrey, J. R. R., and Liburdy, J. A. (1986) "Mean Flow Characteristics of a Turbulent Offset Jet." *ASME. J. Fluids Eng.* March 1986; 108(1): 82–88. doi: <https://doi.org/10.1115/1.3242548>
- Rathore, SK and Das, M.K. (2013) "Comparison of two low-Reynolds number turbulence models for fluid flow study of wall bounded jets", *International Journal of Heat and Mass Transfer*, 61, pp. 365-380. doi: 10.1016/j.ijheatmasstransfer.2013.01.062.
- R.I. Karlsson, J. Eriksson, J. Persson (1992) "LDV measurements in a plane wall jet in a large enclosure", 6th International Symposium on Applications of Laser Techniques to Fluid Mechanics, Lisbon, 1992, pp. 151–156. doi:10.1007/978-3-662-02885-8_19
- Rohatgi A. Web Plot Digitizer; 2015. Available from: <https://apps.automeris.io/wpd/>. [Last accessed on 2022 August 17].
- Rostamy, N., Bergstrom, D.J. and Sumner, D. (2011) "An Experimental Study of a Turbulent Wall Jet on Smooth and Transitionally Rough Surfaces", *Journal of Fluids Engineering*, 133(11). doi: 10.1115/1.4005218.
- S. C. Godi, A. Pattamatta, and C. Balaji. (2019) "Effect of the inlet geometry on the flow and heat transfer characteristics of three-dimensional wall jets," *J. Heat Transfer* 141, 112201, <https://doi.org/10.1115/1.4044509>
- Shih, T.H, Liou, W. W, Shabbir, A , Yang, Z , and Zhu, J. (1995) "A New $k - \varepsilon$ Eddy-Viscosity Model for High Reynolds Number Turbulent Flows - Model Development and Validation", *Computers Fluids*, 24(3):227-238 [https://doi.org/10.1016/0045-7930\(94\)00032-T](https://doi.org/10.1016/0045-7930(94)00032-T)
- Sforza, P.M. and Herbst, G. (1970) "A study of three-dimensional, incompressible, turbulent wall jets," *AIAA J.* 8, 276–283 , <https://doi.org/10.2514/3.5656>
- Speziale, C.G. and Thangam, S. (1992) "Analysis of an RNG based turbulence model for separated flows", *International Journal of Engineering Science*, Vol.30, No.10, pp. 1379-1388 [https://doi.org/10.1016/0020-7225\(92\)90148-A](https://doi.org/10.1016/0020-7225(92)90148-A).
- Tahsini, A.M. (2011) "Assessment of the Accuracy of Spalart-Allmaras Turbulence Model for Application in Turbulent Wall Jets", *World Academy of Science, Engineering and Technology, Open Science Index* 49, *International Journal of Aerospace and Mechanical Engineering*, 5(1), 1 - 6.
- Tang, Z., Rostamy, N., Bergstrom, D.J., Bugg, J.D., and Sumner, D. (2015) "Incomplete similarity of a plane turbulent wall jet on smooth and transitionally rough surfaces", *Journal of Turbulence*, 16:11, 1076-1090, doi:10.1080/14685248.2015.1054034
- Tailland, A., Contribution à l'étude d'un jet plan dirigé tangentiellement à une paroi plane, Doctoral Thesis, Université de Lyon, 1970.
- Yang, Z. and Shih, T.H. (1993) "New time scale based $k-\varepsilon$ model for near-wall turbulence", *AIAA Journal*, 31:7, 1191-1198, doi: <https://doi.org/10.2514/3.11752>

- Wilcox, D. C. (2008) "Formulation of the $k-\omega$ Turbulence Model Revisited", AIAA Journal, Vol. 46, pp. 2823–2838, doi:10.2514/1.36541
- Wilcox, D.C. (2006) "Turbulence Modeling for CFD". 3rd Edition, DCW Industries, Canada, CA, USA